Progress in Additive Manufacturing (2025) 10:11165–11189
https://doi.org/10.1007/s40964-025-01280-5

RESEARCH

Laser percussion micro-drilling on PBF-LB/M-manufactured CoCrMo alloy plates: process characterisation and comparison with additively manufactured holes

Davide Morello[1] · **Silvio Genna**[2,3] · **Claudio Leone**[1,3]

Received: 13 May 2025 / Accepted: 27 July 2025 / Published online: 3 August 2025

Abstract

The paper deals with the laser micro-drilling of CoCrMo superalloy sheets, 1.5 mm in thickness, manufactured via powder bed fusion by laser beam melting (PBF-LB/M) technology, by percussion drilling techniques. Laser drilling tests were carried out using a 450/4500 QCW pulsed fiber laser with a pulse power of up to 4.5 kW. The experimental tests were performed adopting a Box-Behnken design. During the tests, the pulse power, pulse duration, assistant gas pressure, focus position, and total released energy were varied. Hole geometries were characterised at the beam entrance and exit by adopting a 3D digital microscope. The entrance and exit diameters, roundness, taper angle, spatter area, and maximum dross height were analysed. ANalysis Of VAriance (ANOVA) and Response Surface Methodology (RSM) were adopted to investigate the influence of the process parameters and model the process. The geometrical characteristics of the laser-drilled holes were compared to additively manufactured ones. Multi-Objective-Optimization (MRO) was adopted to identify optimal process conditions to produce micro-holes with an imposed diameter and minimal taper angle. Then, the RSM model was experimentally validated, showing a strong correlation with predicted values up to 600 µm. Moreover, the geometry of additively manufactured holes was characterised too, and the mechanisms of defect generation were discussed. From the result, comparing the geometry of the laser-drilled holes to the ones obtained by additive manufacturing, the former technique is particularly competitive in the diameter range of 300–600 µm.

Keywords Additive manufacturing · PBF-LB/M · Micro holes · Percussion drilling · Superalloy

1 Introduction

Metal additive manufacturing (AM) has garnered substantial interest across various industrial sectors that demand highly optimised and customised components, enabling the possibility of overcoming the design constraints inherent to traditional manufacturing methods, and allowing the production of lightweight and complex structures. For instance, it facilitates the fabrication of intricate internal features, such as internal channels, holes and features highly sought after in applications like injection nozzles, heat exchangers, and conformal cooling systems. These capabilities contribute to cost-efficiency by allowing the production of complete parts and lattice structures in a single build, reducing both assembly time and material waste [1–5]. Among different AM processes, powder bed fusion and directed energy deposition are commonly commercially used for metals. Several alloys, such as stainless steel, Aluminium alloys, Titanium, Nickel-based superalloys, and CoCrMo can be adopted [6, 7]. Thanks to their mechanical properties, which are preserved at high temperatures, their corrosion and wear resistance, and biocompatibility [8, 9], Cobalt-base alloys have been adopted in various industrial fields, including the nuclear and aerospace industries [10], and the biomedical field [11, 12]. Despite the advantages of Metal Additive Manufacturing, the process still presents several issues in terms of surface

✉ Davide Morello
davide.morello@unicampania.it

✉ Claudio Leone
claudio.leone@unicampania.it

Silvio Genna
silvio.genna@uniroma2.it

[1] University of Campania Luigi Vanvitelli, Aversa (Ce), Italy

[2] University of Rome Tor Vergata, Rome, Italy

[3] CIRTIBS Research Centre, Aversa (Ce), Italy

quality (roughness) [13], geometrical deviation between the "as-designed" and the "as-built" [14], and the presence of defects such as porosity, splash, balling or semi-melted powders, especially for powder bed fusion processes [6, 15]. These defects make it challenging to create internal features, such as holes, with an adequate level of accuracy, especially those with a nominal diameter of less than 1 mm and a high aspect ratio. In recent years, efforts have been made to produce very tiny holes (with a diameter less than 0.6 mm) with complex shapes (fan-shaped holes) and low roughness for thermo-fluid-dynamics applications through powder bed fusion by laser beam melting (PBF-LB/M). However, the components obtained are generally affected by geometrical defects (geometrical deviation from the as-designed), internal surfaces and entry/exit sections collapsing, and high roughness, which have a significant impact on thermodynamic performance [16, 17]. Then, to overcome the defects due to the AM techniques, compensation strategies or AM parameters optimisation were adopted. For instance, to produce correct micro-holes (with a nominal diameter ranging between 300 and 500 µm, and different length to diameter ratios), Min et al. [14] placed the axis along the building direction and compensated for the diameter. However, since different factors must be considered during the component topologically optimisation, the hole axis placement along the building direction may not be feasible. Moreover, the micro-holes are often placed in directions.

To overcome these limitations, some researchers focused on post-processing treatments to improve the surface quality and accuracy of AM holes, such as mechanical finishing [18], Electro-Discharge machining [19], and Electro-Chemical Processing [14]. Although it is possible to improve the surface quality, the most cost-effective strategy remains to drill the feature directly on the additively manufactured part. Recent research focused on the effect of conventional mechanical drilling on different metal alloys fabricated through PBF-LB/M) [20–24]. However, machining materials with high mechanical properties (such as Titanium, Cobalt, and Nickel alloys, high-strength and heat-resistant steels) causes several problems in terms of chip formation and removal, tool wear, heat generation and reduced cutting speed.

Gatto et al. [10] demonstrate the feasibility of adopting electro-discharge drilling on cobalt-chromium-molybdenum (CoCrMo) alloy parts produced via PBF-LB/M. However, the process presents limited efficiency for small holes in terms of drilling speed. In addition, the adoption of ultrasonic-assisted drilling was studied on additively manufactured titanium alloy [22] and stainless steel [25]. It was demonstrated that the process is suitable for high-quality drilling with minimal thermal impact, extended tool life, and improved hole integrity in AM metals. Nevertheless, its effectiveness decreases with very tiny hole diameters due to limited chip evacuation space, vibration amplitude constraints, increased tool wear and breakage risk.

Laser drilling represents a valid alternative to the previously mentioned methods for creating internal features, such as holes, in additively manufactured components. This process utilises highly focused laser beams to generate holes through mechanisms such as melting and/or vaporisation of the material, depending on the specific drilling technique employed. Thanks to its high precision, consistency, and rapid drilling rates, it finds widespread application in industrial fields such as aerospace, automotive, and medical. Additionally, it enables the production of high-precision, high-aspect-ratio holes in a diverse range of materials, including both conductive and non-conductive substances, as well as brittle and hard materials like superalloys and ceramics [26]. Generally, it is possible to identify different laser drilling methods: single pulse drilling, percussion drilling, trepanning and helical drilling [27, 28]. Upon different pulse durations (long, short and ultrashort pulses) and drilling methods, the material removal mechanisms change, and it influences the formation of the hole, both in terms of quality and productivity (e.g., drilling speed and production capacity) [29]. In laser percussion drilling, the formation of a hole is achieved through the sequential removal of material by a series of laser pulses. The process is governed by parameters such as pulse duration and pulse frequency, which determine the energy delivered to the material and, consequently, the volume ejected for each pulse. However, the quality of the drilled holes is affected by geometrical defects like hole roundness, tapering, and barrelling and by the presence of spatter, dross, burr, recast layer and heat-affected zone. To guarantee adequate hole quality, researchers focused the studies on the effect of different process parameters on the hole quality and their optimisation. [30–36]. Although laser percussion drilling was deeply investigated on several materials, a lack of knowledge was found concerning the process applied to additively manufactured components. In [37], it was explored how laser engraving affects cold-rolled and additively manufactured AISI 316L stainless steel sheets. Both materials were drilled by adopting a nanosecond pulsed fiber laser, and key parameters such as hole diameters, material removal rates, burn width, and hole taper were analysed. While the results showed minimal differences in efficiency between the two types of steel, the additively manufactured sheets (produced via powder bed fusion) exhibited a wider burn area and the presence of noticeable microstructural defects (powder particles near the surfaces of the object that are not fully fused to the surrounding material). In [38], the authors introduce a novel manufacturing technique that integrates AM using continuous-wave (CW) laser-based powder bed fusion with subtractive processes employing ultrafast laser ablation. The

study shows that it is possible to achieve high precision and smooth surfaces by applying ultrafast laser machining during the single-layer deposition. This hybrid approach enables the creation of intricate features with high aspect ratios and significantly improves surface quality, expanding the potential of laser-based manufacturing technologies.

However, in actual industrial fields, the main requirements for drilling operations are the respect of the geometrical and metallurgical constraints, low cost and high productivity. On the other hand, since in laser drilling processes there is no physical tool (as for mechanical drilling), and the hole's geometry depends on the process parameters and material properties, to obtain holes that comply with the requirements, process models are required. This paper, therefore, addresses two points: the issue encountered in AM during the micro-holes production, their geometric characteristics, and the mechanisms of defect production, as well as an analysis and a statistical modelling of the laser percussion drilling process.

To these aims, plates of CoCrMo superalloy, 1.5 mm in thickness, were manufactured via powder bed fusion by laser beam melting (PBF-LB/M). Micro-holes with a nominal diameter (i.e. as designed) of 550 µm, 650 µm, and 750 µm were produced directly during the AM process, with the axis placed orthogonal to the direction of growth. The geometries of the AM micro-holes were then characterised, and the defect mechanisms were assessed. Then, on the same plates, micro-holes were carried out through laser percussion drilling. The drilling tests were performed through a 450/4500 Quasi Continuous Wave (QCW) pulsed fiber laser, characterised by a small beam diameter and a pulse power of up to 4.5 kW. The experimental tests were carried out adopting a Box-Behnken design. The pulse power, pulse duration, assistant gas pressure, focus position, and total released energy were varied during the tests. The entrance and exit diameters, the roundness, taper angle, spatter area, and maximum dross height were analysed. The influence of the process parameters was studied through ANalysis Of VAriance (ANOVA), while Response Surface Methodology (RSM) was used to model the process. Multi-Objective-Optimization (MRO) was adopted to identify optimal process conditions to produce micro-holes with an assigned diameter and a minimal taper angle, and to validate the RSM model. The geometrical characteristics of the laser-drilled holes were compared to additively manufactured ones.

2 Material, equipment, and procedures

2.1 Materials

The experimental tests were carried out on CoCrMo superalloy plates, 1.5 mm in nominal thickness, obtained by PBF-LB/M. A standard powder, EOS CobaltChrome MP1 [39], was adopted for the plate fabrication. This alloy has good corrosion resistance and high mechanical properties, even at elevated temperatures (500–100 °C). Moreover, it has a low nickel percentage and shows a fine, uniform crystal grain structure. These properties are suitable for several applications in the aerospace and medical fields. The plates were produced by the EOS M 290 system, adopting the standard process parameters [40]. The main properties and the chemical composition of CobaltChrome MP1 alloy are reported in Table 1 [41].

Table 1 Main properties and chemical composition of MP1 powder [39, 41]

Main Properties	Symbol	Values	Unit
Yield strength[a]	σ_y	630–640	MPa
Tensile strength[a]	σ_s	1130–1140	MPa
Modulus of elasticity[a]	E	205–208	GPa
Elongation at break[a]	A	28–32	%
Density	ρ	≥ 8300	kg/m^3
Generic particle size distribution	–	15–45	µm

Chemical composition (UNS R31537, ISO 5832–4, ASTM F75, ISO 5832–12, ASTM F1537)

Element	Symbol	Wt %	Element	Symbol	Wt %
Cobalt	Co	Balance	Iron	Fe	0.75
Chromium	Cr	27–30	Manganese	Mn	1
Molybdenum	Mo	5–7	Silicon	Si	1
Tungsten	W	0.2	Carbon	C	0.14
Nickel	Ni	0.1			

[a]heat-treated, according to ISO6892-1

2.2 Equipment

The experimental micro-drilling tests were executed with a 450 W QCW Yb:YAG fiber laser (IPG YLR-450/4500-QCW-AC) working at the fundamental wavelength λ = 1070 nm. The laser works in both continuous wave (CW) and pulsed wave (PW) with a maximum average power released of 450 W (P_{avg}); however, in PW mode it can release pulse power (P_p) up to 4500 W, with the following limitation: the average power cannot exceed the nominal value in CW mode (450 W) and the duty cycle (δ) (i.e. the product of the frequency, *f*, per pulse duration, D) cannot exceed 50%. Thus, considering the well-known equations relating the average power, the pulse energy (E_p), the pulse power and the duty cycle (δ) [42]:

$$E_p = P_{avg}/f \quad (1)$$

$$P_p = E_p/D \quad (2)$$

$$\delta = 100\, f \cdot D \quad (3)$$

The effective process conditions, where the laser can work in PW mode, result in the working area shown in Fig. 1.

Although, QCW laser sources' limitation, compared to the modulated wave (MW) fiber sources with equal pulse power or the pulsed Nd:YAG sources, the QCWs offer several advantages, such as low investment cost, high wall-plug efficiency, reliability, zero maintenance, and high stability. Moreover, the possibility of adopting output small diameter fibres results in a high-quality beam ($BPP = \lambda M^2/\pi = 2.4$ mm × mrad, $M^2 = 2.2$) and small diameters at the focussing point, regardless of the high pulse power. Thanks to their characteristics, these types of sources are often adopted to replace the conventional pulsed

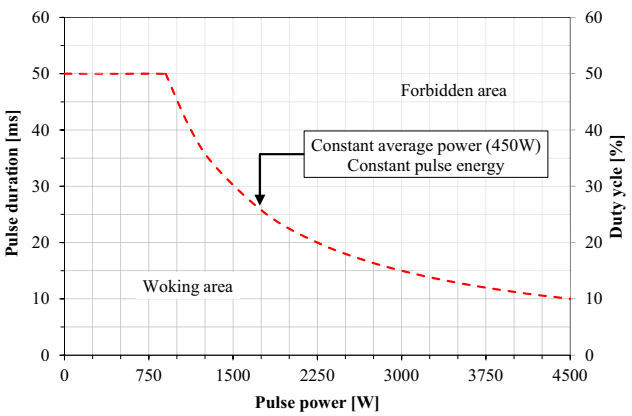

Fig. 1 Working area for PW regime in terms of pulse duration and duty cycle

Nd:YAG and fibre laser in all those operations where high brightness and small spots are required, such as laser welding of reflective materials, micromachining operations [43, 44], and, of course, micro-drilling [45] in actual industrial fields.

A cutting head (IPG MICRO CUTTING HEAD P21-010105 D25) with a 0.8 mm nozzle and a focusing lens of 100 mm in focal length was adopted. The theoretical beam spot diameter (ds) is about 80 µm. The CNC is controlled via a Siemens (Sinumerik™ 802D) programmable logic controller (PLC). The latter allows the cutting patterns execution, the selection of the cutting speed, and the laser On/Off. The laser parameters are working mode (CW or PM), pulse power (P_p), pulse duration (D), pulse frequency (*f*), etc. and are selected through the in-board laser interface. The laser equipment was mounted on a 3 + 1-axis CNC system (Rofin finecut Y 340 M) controlled by the PLC. In Table 2, the main characteristics of the laser source are reported.

2.3 Procedures

2.3.1 Laser drilling

The experimental plan was developed by adopting a systematic approach to the Design of Experiment (DoE) methodology. Compared to the typical approach "one-factor-at-a-time", the DoE approach has different advantages: it reduces the experimental runs, providing information about the main effects and the interaction between the various process parameters [46, 47]. Typically, the DoE approach is not limited to the selection of the test plan (i.e. the factorial plan

Table 2 Laser source specifications

Characteristic	Symbol	Units	Value
Wavelength	λ	nm	1070 ± 5
Mode of Operation		–	CW/PW
Nominal average power[a]	P_{avg}	W	450
Max. pulse power[b]	P_p	W	4500
Max. pulse energy[b]	E_p	J	45
Pulse duration[b]	D	ms	0,05–50
Modulation frequency[b]	f	kHz	0–50
Beam Parameter Product[d]	BPP	mm × mrad	2.4
Output fiber core diameter	OFD	µm	50
Focal length of the collimator	F_c	mm	85
Focal length of the focusing lens	F_F	mm	100
Focussed spot diameter[c]	d_0	µm	80
Power consumption[d]	–	kW	1.8

[a]Max. average power in CW or PW mode

[b]In PW mode

[c]Theoretical values [48]

[d]As declared by the producer

type) since it involves the selection of the control factors (i.e. the settable process parameters that affect the drilling process) and their levels, the response variables as well as the knowledge and the bibliography analysis. The selection of the control factors (i.e. the settable process parameters that affect the drilling process) and the response variables (the measured quantity that describes the hole characteristics) is a critical issue since several factors affecting the process are present, as reported in Fig. 2.

In the present work, the control factors and their levels were selected based on the relevant bibliography, previous experiences, preliminary tests, and the scope of the present work. Moreover, since the present work is a screening phase, to avoid experimental plans that are too complex or large, and reduce the number of tests, the tests were carried out using the laser in a pulsed regime (PW), and fixing some factors according to the following consideration: since the stand-off distance (SOD) is challenging to fine setting, it was fixed at the standard value for the adopted head (1 mm), to avoid combustion phenomena (due to atmospheric O_2), nitrogen (N_2) was adopted as assistant gas for all the tests, in addition, to ensure comparable heating phenomena during the laser drilling operations and to ensure the fast drilling characteristic of laser trepanning is not lost, the drilling time was imposed at 1 s.

Due to the complexity of the phenomena occurring during laser machining, the experimental plan was developed by adopting the Response Surface Methodology (RSM). RSM has the advantage of providing a quadratic regression model (i.e. a set of quadratic equations) that relates the control factors and their products to the response variables. Moreover, the analysis provides the statistically significant control factors (through the ANalysis Of VAriance, ANOVA), the main effect and the interaction plots. Moreover, a Box-Behnken design (BBD) was adopted to reduce the experimental runs. This is a type of experimental plan that does not contain an embedded factorial or fractional factorial design. The treatment combinations of the box-Behnken design are at the midpoints of the edges of the experimental space and require at least three factors. These designs allow an efficient estimation of the first- and second-order coefficients [49] by testing a limited number of conditions (here 46 instead of 243). Because these designs have fewer design points, they are less expensive to run than central composite designs with the same number of factors; consequently, it is often adopted by scholars, in addition to multicriteria optimisation, for process analysis and optimisation [50–52]. On the other hand, since they do not have an embedded factorial design, they are not suited for sequential experiments (i.e. further points to the plan addition). As control factors, the pulse power (P_p), the pulse duration (D), the gas pressure (G_p), the focus position (F, with F that is positive inside the sample and negative above the sample's surface) and the total released energy (E_{tot}) were adopted. The latter is selected by varying the pulse frequency. In Tables 3 and 4, the design summary and the factors and levels of the experimental plan are reported, respectively. In Table 5 the design table is reported together with the physical values of process parameters. The plan was replicated three times in the corner points and six times in the center point (for a total number of tests equal to $46 \times 3 = 138$). In addition, to avoid heat accumulation

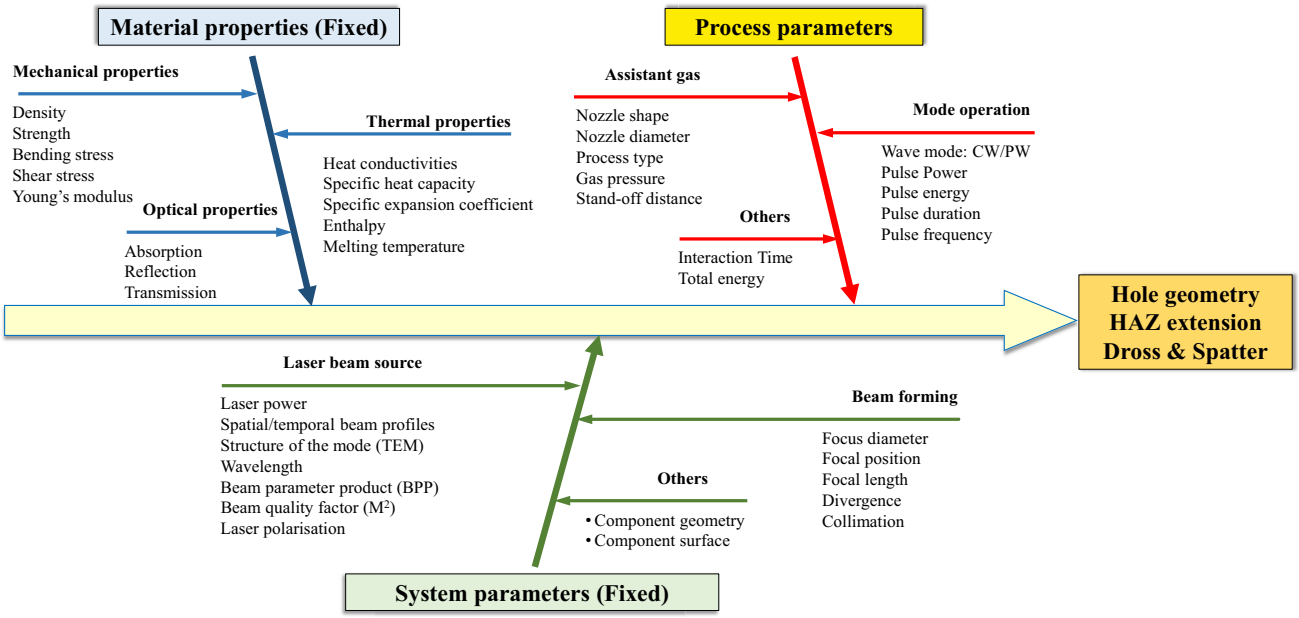

Fig. 2 Parameters affecting the hole geometry and quality

Table 3 Box-behnken design: design summary

Factors:	5	Replicates:	3
Base runs:	46	Total runs:	138
Base blocks:	1	Total blocks:	3
Center points:	18		

Table 4 Experimental plan: factors and levels

Factor	Symbol	Unit	Level		
			− 1	0	1
Pulse power	P_p	kW	3	3.75	4
Duration	D	ms	0.2	2.1	4
Gas Pressure	G_p	bar	7	10	13
Focus position	F	mm	− 2	0	2
Total released energy	E_{tot}	J	60	120	180

around two consecutive holes, the trials were randomised in position by adopting a zig-zag strategy according to the schematic reported in Fig. 3. It is worth noting that the levels (values) adopted were selected based on the preliminary tests, according to the equipment specifications (for instance the maximum gas pressure must be less than 15 bar) and that to avoid blind holes (pulse duration less than 0.2 ms were excluded since they did not allow the formation of through holes for all the control factors combinations).

2.3.2 Hole characterisation

For the hole characterisation, the spatter dimension (i.e. the area of the spatter), the dross height, the taper angle, the inlet and outlet diameter and their roundness, were adopted as response variables. The diameters and roundness were measured, after the dross and spatter elimination through abrasive paper polishing (with 60, 120, and 180 grit), by 8-point interpolation (at intervals of 45° along the circumference) adopting the Least-Squares Method (LSM) for the evaluation of the diameter and the difference between the maximum and minimum radial deviations for the circumference (according to the definition of ISO 1101 2017 Standard). Then, null roundness means a perfect or a regular hole, while high roundness means an irregular hole. The Taper angle was calculated according to Eq. (4), assuming that the centres of the diameters on the two faces were perfectly aligned.

$$\mathrm{Ta} = \mathrm{Tan}^{-1}\left(\frac{D_{in} - D_{out}}{2 \bullet \mathrm{Thickness}}\right) \tag{4}$$

In Table 6, the response variables are reported together with their nomenclature, while in Fig. 4 the schematic of a hole and the measured quantities are reported.

In addition, holes with a nominal diameter of 550 µm, 650 µm and 750 µm were produced on the same plates adopted for the laser drilling test, directly during the manufacturing process (PBF-LB/M) with the axis placed orthogonal to the direction of growth and adopted as reference. For each diameter size, 16 holes were measured in terms of inlet and outlet diameter and their roundness, adopting the same procedure as assumed for the laser trepanned holes. Moreover, for these holes, the percentage error was calculated according to the following equation:

$$\mathrm{Error}\,[\%] = 100\left(\frac{\mathrm{Roundness}}{\mathrm{Diameter}}\right) \tag{5}$$

The percentage error, as the roundness, is a weighted index of how much the hole geometry differs from the hole itself. After measuring the diameters, several holes were separated by laser cutting, paying attention to not overheating the samples, sectioned, and polished with abrasive paper up to 2000. Then they were observed through optical microscopy to verify the internal profile regularity.

2.3.3 Data analysis

After the test, the data were analysed and the statistical significance of the control factors on the response variables was assessed by the ANalysis Of VAriance (ANOVA). The effects of the control factors were studied through the main effects and interaction plot analysis. The ANOVA was carried out with a confidence level of 95% ($\alpha = 0.05$). A control factor is statistically significant if the p-value is less than 0.05. Interaction (p-value < 0.05) occurs when the effect of a control factor on the response variables depends on the level (value) of the other control factor. In addition to the p-value, it was also considered the F-value index. The latter indicates the weight of the effect: the greater the F-value, the greater the variation of the response variables at the control factors' change. Before the analysis, the ANOVA assumptions were verified by the graphical examination of residuals, according to what was reported in [46]. It is worth noting that, since the roundness does not satisfy the residual normality required by the ANOVA assumptions, it was necessary to adopt the Box-Cox transformation, that is a technique (a power function applied to the data) often adopted to stabilise variance and make the data more normal distribution-like.

Then, a full quadratic model was obtained using the Response Surface Methodology (RSM) for each response variable. Optimal process conditions to obtain holes with an imposed diameters (300 µm, 400 µm, 500 µm, and 600 µm) were found by multi-response optimisation (MRO) techniques. Finally, the optimal process conditions were adopted to validate the statistical model and the laser process potentialities.

Table 5 Design Table (non-randomised) and physical values of process parameters

Std.Order	PtType[a]	Levels					Levels (actual values)				
		A	B	C	D	E	P_p [kW]	D [ms]	G_p [bar]	F [mm]	E_{tot} [J]
1	1	− 1	− 1	0	0	0	3	0.2	10	0	120
2	1	1	− 1	0	0	0	4.5	0.2	10	0	120
3	1	− 1	1	0	0	0	3	4	10	0	120
4	1	1	1	0	0	0	4.5	4	10	0	120
5	1	0	0	− 1	− 1	0	3.75	2.1	7	− 2	120
6	1	0	0	1	− 1	0	3.75	2.1	13	− 2	120
7	1	0	0	− 1	1	0	3.75	2.1	7	2	120
8	1	0	0	1	1	0	3.75	2.1	13	2	120
9	1	0	− 1	0	0	− 1	3.75	0.2	10	0	60
10	1	0	1	0	0	− 1	3.75	4	10	0	60
11	1	0	− 1	0	0	1	3.75	0.2	10	0	180
12	1	0	1	0	0	1	3.75	4	10	0	180
13	1	− 1	0	− 1	0	0	3	2.1	7	0	120
14	1	1	0	− 1	0	0	4.5	2.1	7	0	120
15	1	− 1	0	1	0	0	3	2.1	13	0	120
16	1	1	0	1	0	0	4.5	2.1	13	0	120
17	1	0	0	0	− 1	− 1	3.75	2.1	10	− 2	60
18	1	0	0	0	1	− 1	3.75	2.1	10	2	60
19	1	0	0	0	− 1	1	3.75	2.1	10	− 2	180
20	1	0	0	0	1	1	3.75	2.1	10	2	180
21	1	0	− 1	− 1	0	0	3.75	0.2	7	0	120
22	1	0	1	− 1	0	0	3.75	4	7	0	120
23	1	0	− 1	1	0	0	3.75	0.2	13	0	120
24	1	0	1	1	0	0	3.75	4	13	0	120
25	1	− 1	0	0	− 1	0	3	2.1	10	− 2	120
26	1	1	0	0	− 1	0	4.5	2.1	10	− 2	120
27	1	− 1	0	0	1	0	3	2.1	10	2	120
28	1	1	0	0	1	0	4.5	2.1	10	2	120
29	1	0	0	− 1	0	− 1	3.75	2.1	7	0	60
30	1	0	0	1	0	− 1	3.75	2.1	13	0	60
31	1	0	0	− 1	0	1	3.75	2.1	7	0	180
32	1	0	0	1	0	1	3.75	2.1	13	0	180
33	1	− 1	0	0	0	− 1	3	2.1	10	0	60
34	1	1	0	0	0	− 1	4.5	2.1	10	0	60
35	1	− 1	0	0	0	1	3	2.1	10	0	180
36	1	1	0	0	0	1	4.5	2.1	10	0	180
37	1	0	− 1	0	− 1	0	3.75	0.2	10	− 2	120
38	1	0	1	0	− 1	0	3.75	4	10	− 2	120
39	1	0	− 1	0	1	0	3.75	0.2	10	2	120
40	1	0	1	0	1	0	3.75	4	10	2	120
41	0	0	0	0	0	0	3.75	2.1	10	0	120
42	0	0	0	0	0	0	3.75	2.1	10	0	120
43	0	0	0	0	0	0	3.75	2.1	10	0	120
44	0	0	0	0	0	0	3.75	2.1	10	0	120
45	0	0	0	0	0	0	3.75	2.1	10	0	120
46	0	0	0	0	0	0	3.75	2.1	10	0	120

0 is the center point.

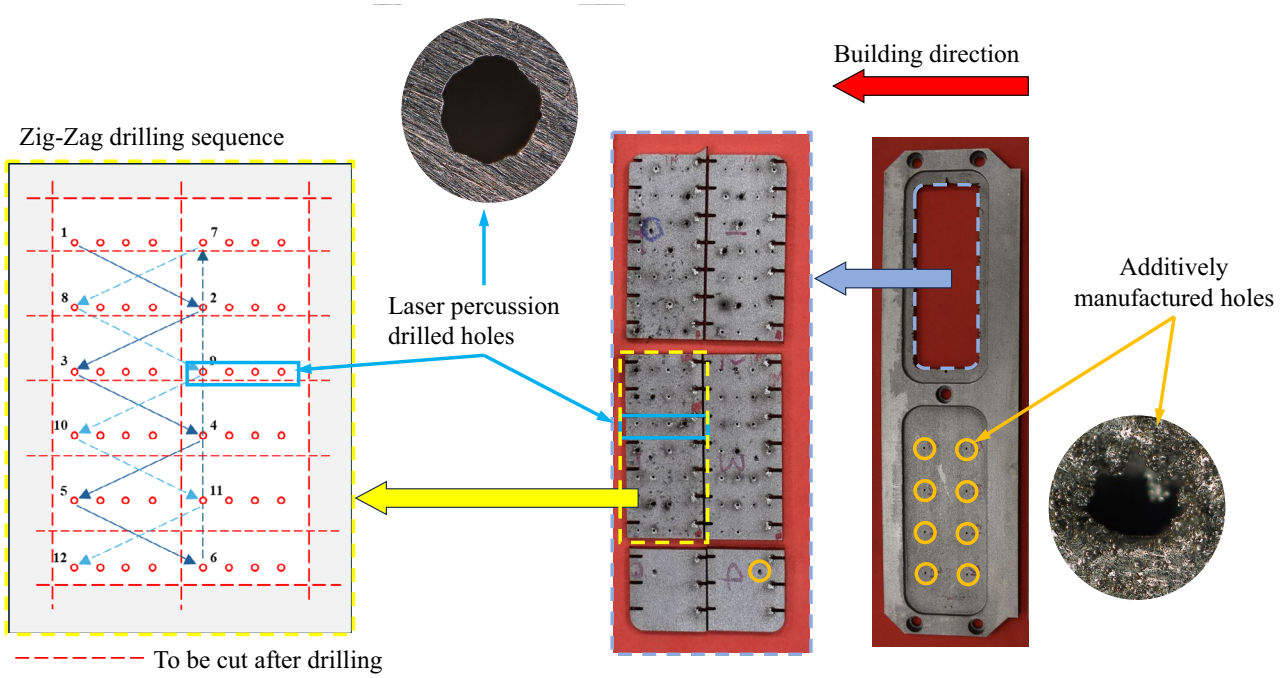

Fig. 3 Schematic of Zig-Zag drilling randomisation and samples after drilling and separation

Table 6 Adopted response variables and their nomenclature

Measuring position	Response variables	Symbol	Unit
Input surface	Input Diameter	D_{in}	µm
	Roundness	R_{in}	µm
	Spatter extension	S	mm^2
Input surface	Output Diameter	D_{out}	µm
	Roundness	R_{out}	µm
	Dross height	Dross	µm
Derived quantity (Eq. 4)	Taper angle	Ta	deg

3 Results

3.1 Characterisations of the holes additively manufactured

Figure 5 shows the measured diameters (Fig. 5a) and the taper angle (Fig. 5b) as a function of the nominal diameter, while the computed values are summarised in Table 7. From Fig. 5a, the nominal diameter overestimates the measured one by a value ranging from 23% for the 550 µm to 15% for the 750 µm, resulting in an effective diameter of $419.8^{\pm 26.3}$, $525.2^{\pm 30.99}$ and $632.8^{\pm 19.03}$ for the nominal diameters of 550 µm, 650 µm, and 750 µm, respectively. Conversely, the taper angle (Fig. 5 b) is very close to 0, varying between $0.228^{\pm 0.732}$ degrees, $0.652^{\pm 0.0.619}$ degrees, and $0.314^{\pm 0.554}$ degrees for the nominal diameters of 550 µm, 650 µm, and 750 µm, respectively, with a standard deviation higher than the mean.

Figure 6 shows the measured diameters (Fig. 6a) and the Error [%] (Fig. 6b). From Fig. 6a, the roundness varies in the range of 20–160 µm. The nominal diameter of 550 µm shows the highest roundness values and standard deviation ($67.77^{\pm 37.55}$ µm). The 650 µm and 750 µm in nominal diameter show a bit smaller value ($51.52^{\pm 19.38}$ µm and $62.01^{\pm 27.95}$ µm, respectively). However, the Error [%] analysis (Fig. 6b) shows that the diameter reduction results in an increase of the error [%] ($16.43^{\pm 9.48}$ µm, $9.78^{\pm 3.59}$ µm, and $9.83^{\pm 4.48}$ µm for the nominal diameters of 550 µm, 650 µm, and 750 µm, respectively). Therefore, although roundness values are comparable, the Error [%] increases as the diameter decreases. Finally, in Fig. 7, the histograms of the diameter and the roundness are reported together with the distribution. From the figure, the diameters show a normal distribution, while the roundness has a lognormal distribution.

Figure 8 shows images of some holes for the three nominal diameters. From the figure, the hole appears elliptical, with the diameter along the building direction smaller than that along the normal direction. The holes are characterised by a significant quantity of particles/particle clusters attached underneath the upper arch, while in the lower arch and at the side parts, a more regular profile with few particles or small particle clusters attached is observed. The same phenomena are observable in the sections, Fig. 9, with the difference that, in addition to clearly seeing the irregularities

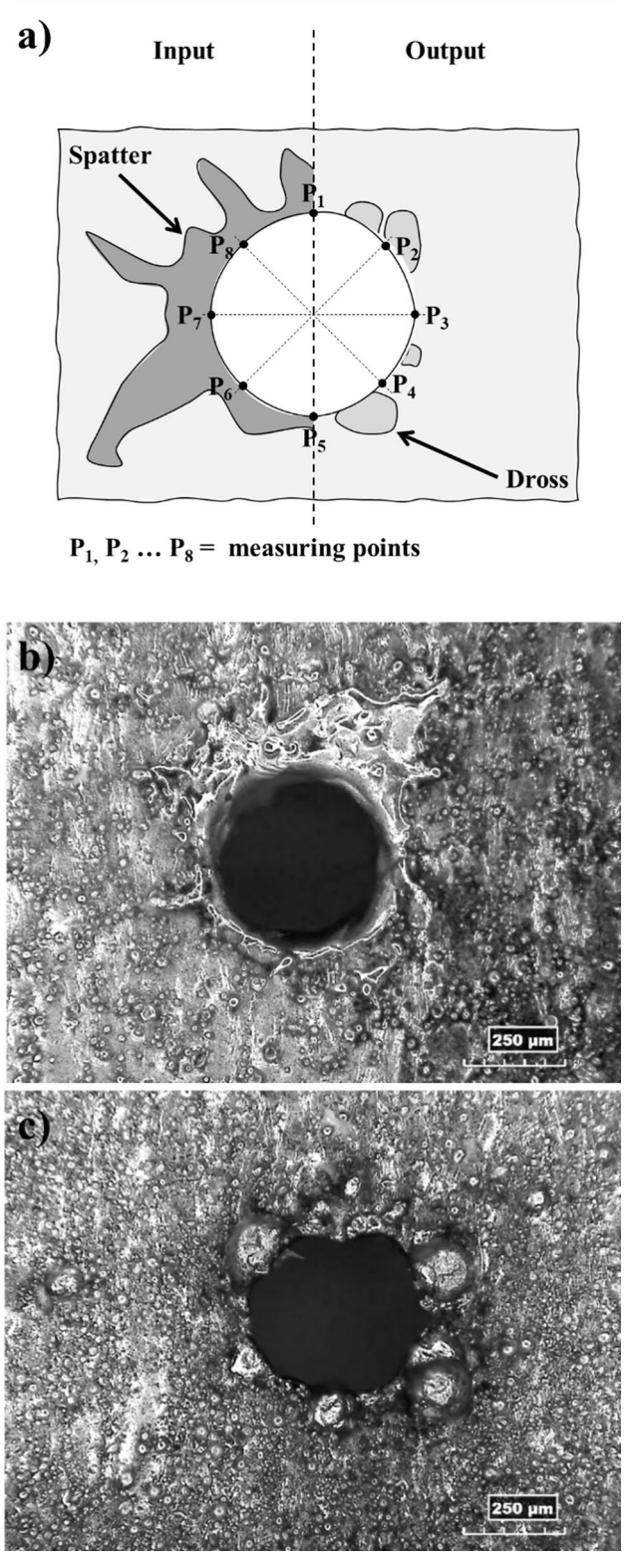

Fig. 4 **a** Schematic of the adopted response variables; Images of a laser-drilled hole at the beam **b** inlet and **c** outlet

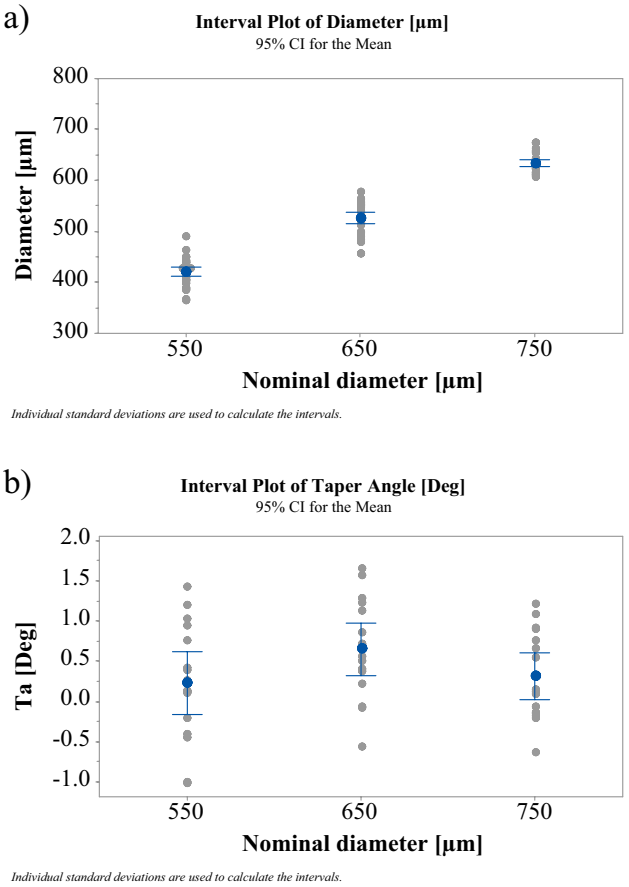

Fig. 5 Interval plot of: **a** Diameter; **b** Taper angle

in the upper and down profiles, the particle clusters at the top of the hole are larger and more visible.

The holes' irregular geometries are due to the different mechanisms involved in the surface creation during the PBF-LB/M process. Generally speaking, there are three main regions in a component produced by PBF-LB/M: the up-skin, the down-skin, and the in-skin. The up-skin refers to the region on the part layer above which there is no area to be exposed (for holes, this is the lower part); the down-skin is the region in contact with the building platform or the unconsolidated particles (for holes, the surface belonging to the upper arch of the hole) subject to laser irradiation; the in-skin is the region where there are above-exposed and below-exposed areas. (see Fig. 10). Moreover, each layer is composed of an external region (the contour) and an inner region (the hatching region). To regulate the mechanical properties and roughness of the part and avoid defects, each region is fabricated by assigning different process parameters such as laser power, scan speed, number of contours (for the contour), and hatching distance (for the hatching region) [53].

During the process, the lower arc and the lateral parts of the hole are in close contact with the consolidated material,

Table 7 Computed values for the Diameter, taper angle, roundness and Error

Nominal diameter [µm]	Diameter [µm]		Taper angle [deg]		Roundness [µm]		Error [%]	
	Mean	St. Dev	Mean	St. Dev	Average	St. Dev	Average	St. Dev
550	419.8	26.30	0.2284	0.7324	67.77	37.55	16.43	9.478
650	525.2	30.99	0.6519	0.6192	51.52	19.38	9.781	3.588
750	632.8	19.03	0.3138	0.5536	62.01	27.95	9.833	4.482

facilitating thermal exchange and resulting in a quasi-well-defined arch (i.e. with a limited number of particles or particle clusters attached), as visible in Fig. 10a, b. Conversely, during the upper arc formation, Fig. 10c, the molten pool is supported by the unmolten particles, which have a thermal diffusivity one order of magnitude lower than the consolidated material. Consequently, the local temperature increases, superheating occurs in the powder bead particles, and the molten materials can infiltrate inside the powder bead, generating the particle clusters attachment, Fig. 10d. This is consistent with then observed by Charles A. et al. during the down-facing surface formation in [54]. Moreover, the annealing process that follows the component production allows a further improvement of the particles' anchorage, which, although they are still recognisable as a particle cluster, becomes one with the component.

The mechanism by which the upper surface is produced highlights the problems that arise when micro-holes are required perpendicular to the building direction. The latter represents an issue for the PBF-LB/M process. Although it is possible to improve the quality of the holes, for example, through an appropriate selection of the process parameters and building direction, as well as geometrical compensation [14, 16, 17], this also represents a limitation since it could impact on other components' characteristics (for instance the roughness or the support number and position).

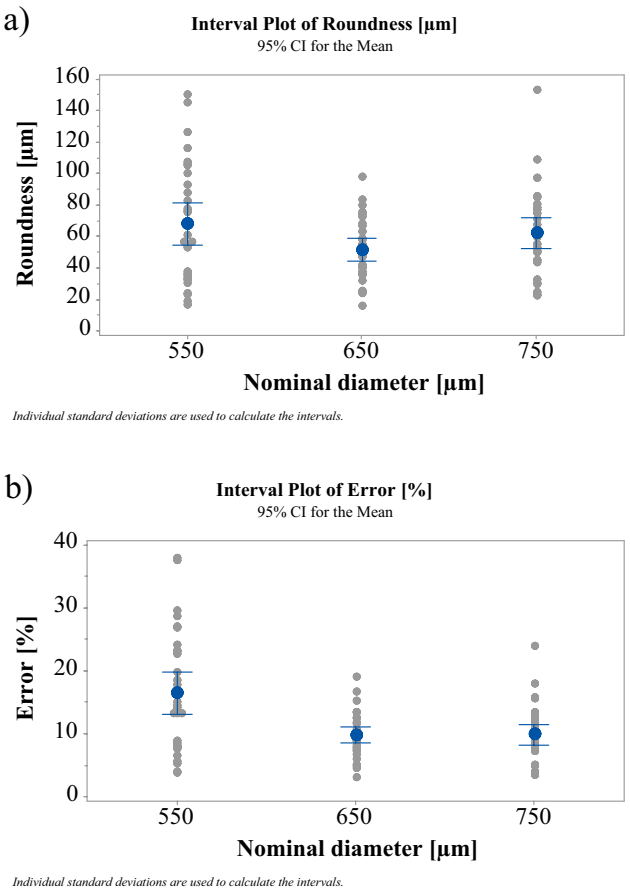

Fig. 6 Interval plot of: **a** Roundness; **b** Error [%]

3.2 RSM model for laser percussion drilling process

3.2.1 ANOVA table

Tables 8 and 9 summarise the analysis showing the significant control factors (p-value < 0.05, which, in the tables, are highlighted by bold text), the F-value, which indicates the weight of the effect: the greater the F-value, the greater the variation of the response variables at control factor change, and the errors performed in the model estimation (the R-sqs index).

From the tables, the pulse power (P_p) affects the D_{out}, and the Spatter (p-value < 0.05); the duration (D) affects all the response variables except the R_{out} and the Ta, the pressure (G_p) does not affect any response variable, while the Focus position (F) affect all the response variables. In addition, since the focus position has an F-value that is an order of magnitude larger than that of the other variables, it is the most influential parameter among all those selected. Finally, the total energy (E_{tot}) affects only the dross height (Dross), even if the p-value appears very close to the confidence level: $\alpha = 0.05$ (p-value = 0.047). The D × F interaction is significant for D_{in}, R_{in}, D_{out}, Ta, and Dross. The presence of quadratic terms indicates the presence of curvatures in the model surfaces. In this regard it should be noted that D^2, affects all the control factors, F^2 affects the D_{in}, R_{in} D_{out}, Ta, and Dross, while $E_{tot}{}^2$ affects D_{in}, R_{in}, Ta, and Dross. Regarding the model estimation, the R-sq [%], R-sq(adj) [%] and the R-sq(pred) [%] were adopted. The R-Sq [%] (R-square or R^2) describes the amount of variation in the observed response that is explained by the control factors; R-sq (adj) [%] is a

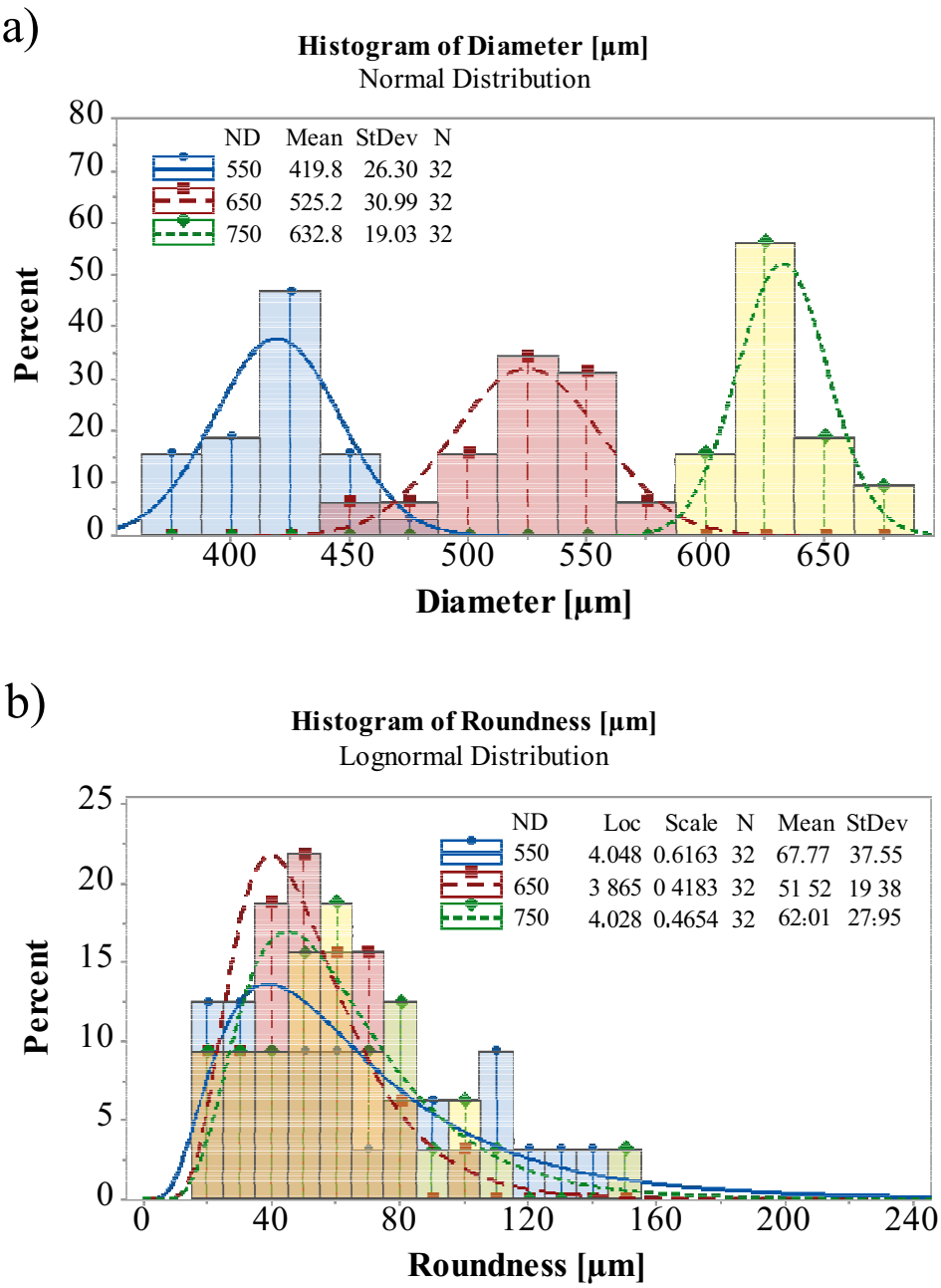

Fig. 7 Histogram of **a** Normal distribution of diameter; **b** Lognormal distribution of Roundness

modified R-Sq [%] that has been adjusted for the number of terms in the analysis, while the R-sq(pred)[%] is related to the error present in the RSM model. From the analysis of Table 8 and Table 9, results that the D_{in} and D_{out} present an R-sq value (R-sq > 95% with less than two percentage points difference between R-sq and R-sq predicted) that permits considering the model well performing. The taper angle shows a barely acceptable value (R-sq = 91% and a difference between R-sq and R-sq(pred) > 2%) that permits to consider the model adequate. Conversely, since R_{in}, R_{out}, Spatter and Dross present significantly lower values (79%, 34%, 74% and 53.16%, respectively), the regression model is not accurate enough to estimate/model the parameter. Then, the effect of the process parameters on R_{in}, R_{out}, Spatter and Dross was studied through the analysis of the main effect plot carried out directly on the experimental data. In addition, since the interactions show F-values one or more orders less than the main factor for the latter process parameters, the interaction plots were discarded from the analysis.

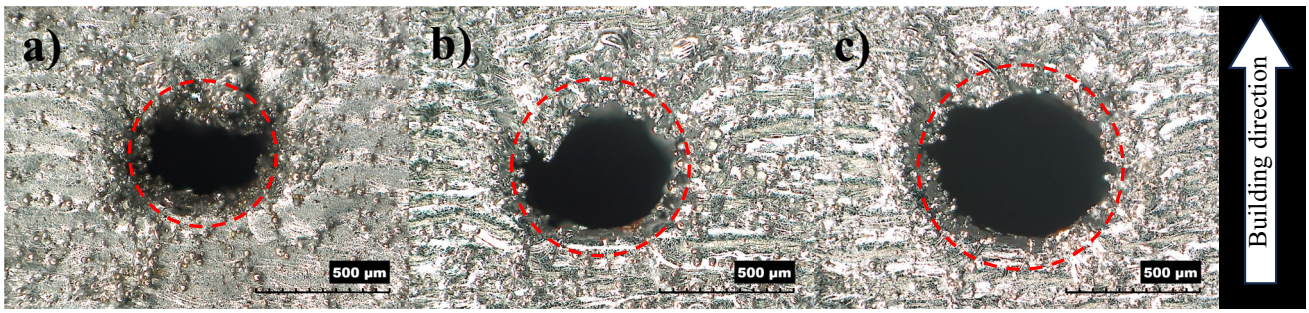

Fig. 8 Typical aspect of the holes additively manufactured for a nominal diameter of: **a** 550 µm; **b** 650 µm; **c** 750 µm. The dashed lines represent the nominal diameter

Fig. 9 Images of hole section for a nominal diameter of: **a** 550 µm; **b** 650 µm; **c** 750 µm

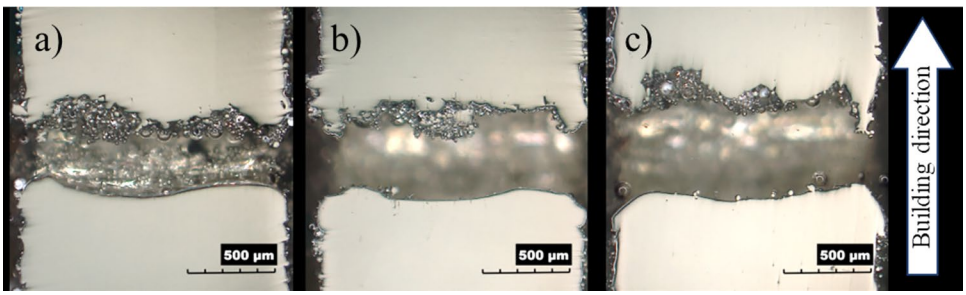

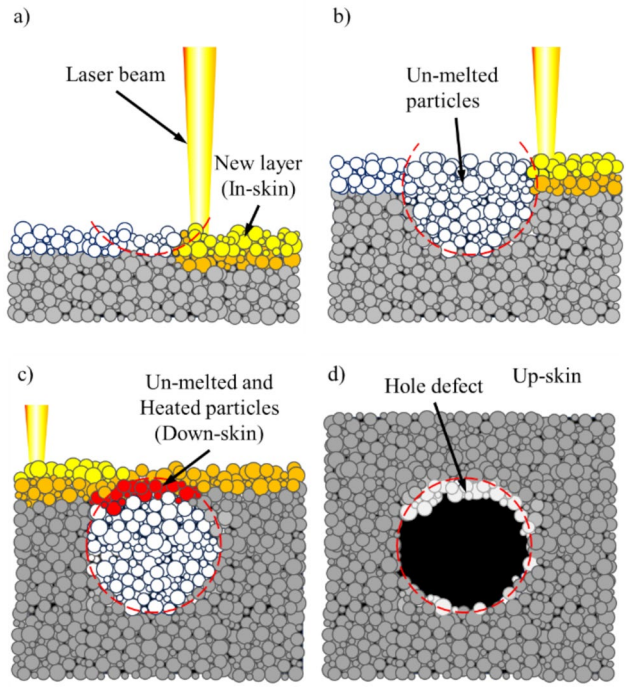

Fig. 10 Schematic of the hole formation (in the image, the particles are out of scale)

3.2.2 The RSM model

As aforementioned, one of the advantages of the Box-Behnken design is the possibility of providing a second-order regression model (i.e. a set of quadratic equations) relating the control factors and their products to the response variables. These equations relate the control factors (P_p, D, F, G_p, and E_{tot}) and their products to the response variables (D_{in}, R_{in}, D_{out}; R_{out}, Ta, Spatter and Dross) by way of 21 constants (K1, K2, …, K21) [49]. The basic equation is the following:

$$\begin{aligned} Source = {} & K1 + K2 \cdot P_p + K3 \cdot D + K4 \cdot G_p + K5 \cdot F \\ & + K6 \cdot E_{tot} + K7 \cdot P_p^2 + K8 \cdot D^2 + K9 \cdot G_p^2 \\ & + K10 \cdot F^2 + K11 E_{tot}^2 + K12 \cdot P_p \times D \\ & + K13\, P_p \times G_p + K14 \cdot P_p \times F + K15 \cdot P_p \times E_{tot} \\ & + K16 \cdot D \times G_p + K17 \cdot D \times F + K18 \cdot D \\ & \times E_{tot} + K19 \cdot G_p \times F + K20 \cdot G_p \times E_{tot} \\ & + K21 \cdot F \times E_{tot} \end{aligned} \quad (6)$$

Where the term "Source" indicates the response variable. Table 10 summarises the equations for the response variables that show an R-sq(pred) [%] value higher than 85%.

Table 8 ANOVA table for D_{in}, R_{in}, D_{out}, and R_{out}

Source	D_{in}		R_{in}		D_{out}		R_{out}	
	F-Value	*p*-value	F-Value	*p*-value	F-Value	*p*-value	F-Value	*p*-value
P_p	2.39	0.125	0.10	0.752	18.40	**0.000**	0.42	0.516
D	102.39	**0.000**	4.92	**0.029**	322.51	**0.000**	1.95	0.166
G_p	1.94	0.166	0.00	0.966	0.24	0.625	1.16	0.284
F	2175.02	**0.000**	296.17	**0.000**	3635.39	**0.000**	35.09	**0.000**
E_{tot}	0.57	0.451	1.28	0.261	6.80	**0.010**	1.53	0.219
P_p^2	0.16	0.689	0.26	0.614	3.87	0.051	2.63	0.107
D^2	43.31	**0.000**	5.43	**0.022**	74.29	**0.000**	**4.05**	**0.047**
G_p^2	1.31	0.255	1.30	0.256	2.89	0.092	0.33	0.567
F^2	272.18	**0.000**	106.44	**0.000**	251.43	**0.000**	0.53	0.468
E_{tot}^2	4.80	**0.030**	14.80	**0.000**	0.97	0.327	0.06	0.811
$P_p \times D$	0.02	0.892	0.05	0.816	0.33	0.569	3.26	0.074
$P_p \times G_p$	1.19	0.277	0.50	0.479	0.47	0.496	0.16	0.692
$P_p \times F$	0.34	0.561	1.84	0.178	4.45	**0.037**	0.49	0.485
$P_p \times E_{tot}$	1.30	0.256	0.47	0.496	0.59	0.443	0.00	0.973
$D \times G_p$	2.62	0.108	0.08	0.784	0.57	0.450	0.01	0.925
$D \times F$	53.90	**0.000**	6.63	**0.011**	62.74	**0.000**	3.31	0.072
$D \times E_{tot}$	0.00	0.946	0.08	0.772	0.89	0.347	0.24	0.623
$G_p \times F$	0.14	0.706	0.91	0.342	0.10	0.747	0.07	0.787
$G_p \times E_{tot}$	0.83	0.364	0.17	0.677	1.97	0.163	0.56	0.455
$F \times E_{tot}$	0.43	0.512	1.15	0.285	0.57	0.450	1.37	0.245
R-sq [%]		96.00		78.99		97.47		34.44
R-sq(adj) [%]		95.23		74.98		96.99		21.89
R-sq(pred) [%]		94.21		69.98		96.36		5.56

3.2.3 Influence of process parameters

Before explaining the main factor and interaction plots, it is necessary to introduce Fig. 11, where the theoretical beam intensity distribution at the inlet and outlet sample surfaces for the three pulse power values (4.5, 3.75, and 3 KW) at the in-focus plane variation (-2 mm, 0 mm, + 2 mm) is reported. In the figure, the radius at the beam focus point (r_0) and the transverse intensity (I(r,z)) were calculated by the following equations [42, 48, 55]:

$$r_0 = \frac{d_0}{2} = OFD \cdot \frac{F_F}{F_c} \tag{14}$$

$$I(r,z) = \frac{P}{\pi r_{0z}^2/2} \cdot \exp\left(-2\frac{r}{r_{0z}^2}\right) \tag{15}$$

where r_0 is the radius at the beam focus point, r_{0z} is the radius at a distance from the beam focus point equal to z, OFD is the output fiber core diameter, F_C is the focal length of the collimator, and F_F is the Focal length of the focusing lens, as listed in Table 2. The radius at the z position (r_{0z}) was obtained by adopting the tool available in [55]. It is worth noting that since the laser beam does not show a theoretical Gaussian distribution (BPP = 2.4, $M^2 = 7$), the equations underestimate the actual radius. However, for the present discussion, this difference can be neglected.

Looking at Fig. 11a, considering the ratio between the maximum and the minimum beam intensity at the pulse power variation, it is possible to notice that, fixing the position and according to Eq. 7, this ratio is 1.5. Conversely, since the focus position controls the effective ratio, the ratio between the maximum and the minimum beam intensity for the different focusing positions is approximately 30. Moreover, at the inlet plane, a defocussing of ± 2 mm results in the same intensity distribution, while at the outlet plane, a significant difference between the two distributions is visible, with the latter being highest at F = + 2. Then, since the ability to drill the component depends essentially on both the energy intensity reached on the input surface and along the entire thickness, it is evident that in the configuration Focus = − 2, the system has a lower possibility of correctly working the material (i.e. producing cylindrical holes).

In Figs. 12, 13 and 14, the main effect plot and the interaction plot for the significant control factors are reported for D_{in}, D_{out}, and Ta. From Fig. 12a, both diameters increase as the focus position (F) increases. This is the most influential parameter since it determines the larger amplitude variation, as confirmed by the highest F-values (see Table 8). However,

Table 9 ANOVA table for Ta, Spatter, and Dross

Source	Ta		Spatter		Dross	
	F-Value	*p*-value	F-Value	*p*-value	F-Value	*p*-value
P_p	0.44	0.510	13.41	**0.000**	2.18	0.142
D	1.53	0.219	10.50	**0.002**	23.84	**0.000**
G_p	1.58	0.212	1.99	0.161	0.02	0.886
F	322.35	**0.000**	258.02	**0.000**	68.63	**0.000**
E_{tot}	0.35	0.555	0.72	0.397	4.43	**0.037**
P_p^2	2.32	0.131	0.15	0.698	0.67	0.415
D^2	6.13	**0.015**	5.82	**0.017**	6.64	**0.011**
G_p^2	0.10	0.754	0.13	0.723	1.00	0.319
F^2	711.88	**0.000**	0.22	0.639	4.76	**0.031**
E_{tot}^2	3.43	0.067	0.64	0.425	0.55	0.460
$P_p \times D$	0.03	0.870	3.64	0.059	0.73	0.394
$P_p \times G_p$	0.68	0.412	1.52	0.221	0.63	0.428
$P_p \times F$	0.27	0.604	0.03	0.855	4.53	0.035
$P_p \times E_{tot}$	0.69	0.408	1.97	0.164	0.30	0.582
$D \times G_p$	1.86	0.176	1.53	0.219	0.55	0.461
$D \times F$	13.53	**0.000**	0.74	0.393	4.16	**0.044**
$D \times E_{tot}$	0.20	0.659	0.07	0.789	0.15	0.698
$G_p \times F$	0.34	0.561	0.18	0.674	0.17	0.679
$G_p \times E_{tot}$	0.05	0.817	0.03	0.869	2.49	0.117
$F \times E_{tot}$	0.09	0.770	1.92	0.169	0.72	0.398
R-sq [%]		91.27		73.70		53.16
R-sq(adj) [%]		89.60		68.44		44.20
R-sq(pred) [%]		87.20		61.63		31.17

Table 10 Regression Equations in Uncoded Units (P_p = kW; D = ms; G_p = bar; F = mm, E_{tot} = J)

$$D_{in} = 581 - 8 \cdot P_p + 73.0 \cdot D - 11.7 \cdot G_p + 82.9 \cdot F - 3.18 \cdot E_{tot} + 6.5 \cdot P_p^2 - 16.57 \cdot D^2 + 1.16 \cdot G_p^2 + 37.49 \cdot F^2 + 0.00553 \cdot E_{tot}^2 - 1.29 \cdot P_p \cdot D - 6.52 \cdot P_p \cdot G_p + 5.22 \cdot P_p \cdot F + 0.341 \cdot P_p \cdot E_{tot} + 3.82 \cdot D \cdot G_p + 25.94 \cdot D \cdot F - 0.008 \cdot D \cdot E_{tot} + 0.85 \cdot G_p \cdot F + 0.0681 \cdot G_p \cdot E_{tot} - 0.074 \cdot F \cdot E_{tot} \quad (7)$$

$$D_{out} = 131 + 150.7 \cdot P_p + 85.1 \cdot D - 17.1 \cdot G_p + 45.1 \cdot F - 0.989 \cdot E_{tot} - 15.90 \cdot P_p^2 - 10.85 \cdot D^2 + 0.858 \cdot G_p^2 - 18.01 \cdot F^2 + 0.00124 \cdot E_{tot}^2 - 2.69 \cdot P_p \cdot D - 2.04 \cdot P_p \cdot G_p + 9.44 \cdot P_p \cdot F + 0.115 \cdot P_p \cdot E_{tot} + 0.89 \cdot D \cdot G_p + 13.99 \cdot D \cdot F - 0.0556 \cdot D \cdot E_{tot} - 0.36 \cdot G_p \cdot F + 0.0523 \cdot G_p \cdot E_{tot} - 0.0424 \cdot F \cdot E_{tot} \quad (8)$$

$$Ta = 8.58 - 3.03 \cdot P_p - 0.236 \cdot D + 0.106 \cdot G_p + 0.719 \cdot F - 0.0418 \cdot E_{tot} + 0.428 \cdot P_p^2 - 0.1085 \cdot D^2 + 0.0055 \cdot G_p^2 + 1.0553 \cdot F^2 + 0.000081 \cdot E_{tot}^2 + 0.027 \cdot P_p \cdot D - 0.086 \cdot P_p \cdot G_p - 0.081 \cdot P_p \cdot F + 0.00431 \cdot P_p \cdot E_{tot} + 0.0559 \cdot D \cdot G_p + 0.2262 \cdot D \cdot F + 0.00091 \cdot D \cdot E_{tot} + 0.0227 \cdot G_p \cdot F + 0.00030 \cdot G_p \cdot E_{tot} - 0.00057 \cdot F \cdot E_{tot} \quad (9)$$

$$\ln(R_{in})^* = 6.00 - 0.35 \cdot P_p - 0.296 \cdot D - 0.042 \cdot G_p - 0.117 \cdot F - 0.0254 \cdot E_{tot} + 0.069 \cdot P_p^2 + 0.0499 \cdot D^2 + 0.00981 \cdot G_p^2 + 0.1995 \cdot F^2 + 0.000083 \cdot E_{tot}^2 - 0.0187 \cdot P_p \cdot D - 0.0360 \cdot P_p \cdot G_p + 0.1033 \cdot P_p \cdot F + 0.00173 \cdot P_p \cdot E_{tot} + 0.0055 \cdot D \cdot G_p + 0.0774 \cdot D \cdot F + 0.00029 \cdot D \cdot E_{tot} + 0.0182 \cdot G_p \cdot F - 0.000265 \cdot G_p \cdot E_{tot} - 0.001022 \cdot F \cdot E_{tot} \quad (10)$$

$$\ln(R_{out})^* = -0.87 + 2.06 \cdot P_p + 0.662 \cdot D + 0.009 \cdot G_p + 0.544 \cdot F + 0.0039 \cdot E_{tot} - 0.215 \cdot P_p^2 - 0.0415 \cdot D^2 + 0.00475 \cdot G_p^2 - 0.0135 \cdot F^2 - 0.000005 \cdot E_{tot}^2 - 0.1393 \cdot P_p \cdot D - 0.0194 \cdot P_p \cdot G_p - 0.0513 \cdot P_p \cdot F - 0.00008 \cdot P_p \cdot E_{tot} + 0.0018 \cdot D \cdot G_p - 0.0526 \cdot D \cdot F + 0.000475 \cdot D \cdot E_{tot} + 0.0050 \cdot G_p \cdot F - 0.000458 \cdot G_p \cdot E_{tot} - 0.00107 \cdot F \cdot E_{tot} \quad (11)$$

$$Spatter = -575{,}444 + 289{,}913 \cdot P_p + 332{,}686 \cdot D + 121{,}741 \cdot G_p + 229{,}350 \cdot F - 4784 \cdot E_{tot} - 25{,}984 \cdot P_p^2 - 24{,}800 \cdot D^2 - 1464 \cdot G_p^2 - 4334 \cdot F^2 - 8.4 \cdot E_{tot}^2 - 75{,}586 \cdot P_p \cdot D - 29{,}431 \cdot P_p \cdot G_p - 6585 \cdot P_p \cdot F + 1848 \cdot P_p \cdot E_{tot} + 11{,}652 \cdot D \cdot G_p - 12{,}144 \cdot D \cdot F - 126 \cdot D \cdot E_{tot} - 3776 \cdot G_p \cdot F + 52 \cdot G_p \cdot E_{tot} + 621 \cdot F \cdot E_{tot} \quad (12)$$

$$Dross = 693 - 92 \cdot P_p - 35.6 \cdot D - 27.8 \cdot G_p + 142.1 \cdot F - 2.60 \cdot E_{tot} + 17.9 \cdot P_p^2 + 8.80 \cdot D^2 + 1.37 \cdot G_p^2 + 6.72 \cdot F^2 + 0.00254 \cdot E_{tot}^2 - 10.9 \cdot P_p \cdot D - 6.44 \cdot P_p \cdot G_p - 25.8 \cdot P_p \cdot F + 0.223 \cdot P_p \cdot E_{tot} + 2.37 \cdot D \cdot G_p + 9.78 \cdot D \cdot F - 0.062 \cdot D \cdot E_{tot} - 1.26 \cdot G_p \cdot F + 0.160 \cdot G_p \cdot E_{tot} - 0.129 \cdot F \cdot E_{tot} \quad (13)$$

*After box cook transformation

it acts differently on the two diameters (as also expected since the quadratic terms have opposite signs). The output diameter (D_{out}) follows the trend of the energy distribution at the exit surface: it increases as the maximum intensity increases and as the distribution narrows (i.e. as F increases, as visible in Fig. 11). For high focus positions, the widening of the Gaussian distribution leads to a reduction of the slope. D_{in} is also strictly related to the Gaussian Distribution;

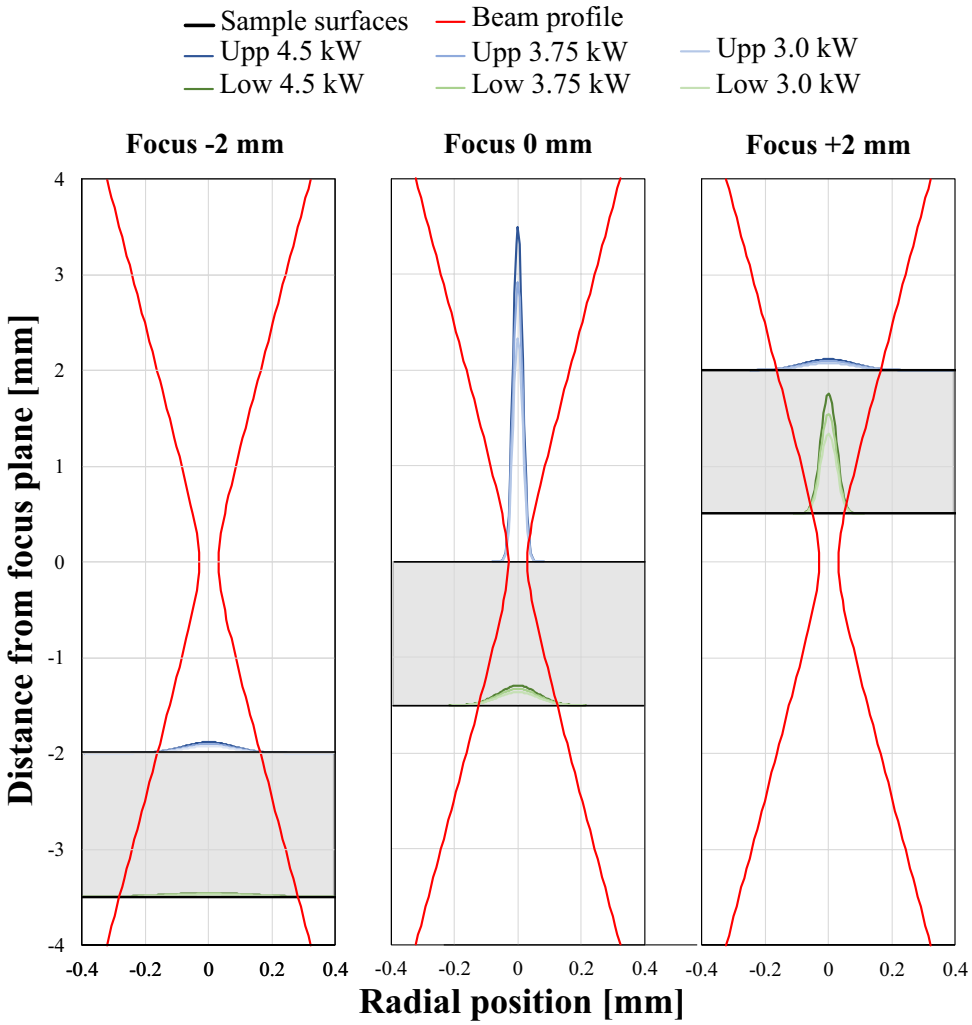

Fig. 11 Effect of focus position and pulse power on the beam intensity distribution at the inlet and outlet sample surfaces

however, since the latter is directly exposed to the radiation and the plasma phase, due to the laser beam-matter interaction, it is less affected by the Gaussian intensity distribution broadening and monotonically increases with the focus position increase. These trends are consistent with what was observed by Yilbas and Sami [56]. In their work, Yilbas and Sami adopt an Nd:YAG to drill with 1.48 ms pulse length, a pulse energy of about 20 J, a focal length of 50 mm on a stainless-steel sheet, 0.7 mm and 1.4 mm in thickness. They observed a direct dependence between the diameter and the laser beam footprint (i.e. to the width of the distribution intensity) in the 4 mm focus variation. However, around zero (focus positioned on the piece), the diagrams show a trend very similar to that observed here.

As a matter of fact, the phenomenon is more complex, and the diameters do not depend only on how the intensity of the radiation is distributed on the two surfaces. Indeed, the area close to the surface is strongly influenced by the presence of the plasma that forms during the laser beam-matter interaction and by how the latter exchanges the thermal energy. From this point of view, the upper surface is closer to both heat sources (direct and plasma radiation) and therefore tends to reduce less when the focus position moves away. It is conceivable to assume that, having sufficient energy (i.e. high P_p and D), even in the present case, for larger variations of the focus (more than ± 2 mm), a similar result would have been obtained. The effect of D, P_p and E_{tot} (these last two only for D_{out}) is simple to explain, their increase involves an increase in the energy made available for material machining and, therefore, the obtained diameters (Fig. 12). On the other hand, since the diameter at the entrance is generated in the first moments of processing and the maximum intensity differs by 50%, the total energy and the pulse power do not affect the D_{in}. Regarding the interactions, Fig. 13, these consist in the fact that the variation in diameter as the duration varies, is greater the denser the distribution of energy. Consequently, both the diameters increase more rapidly at the focus increases when the duration is set at 2.1 or 4 ms.

The behaviours of the Ta, Fig. 14, are a direct consequence of the behaviours of the two diameters. As shown

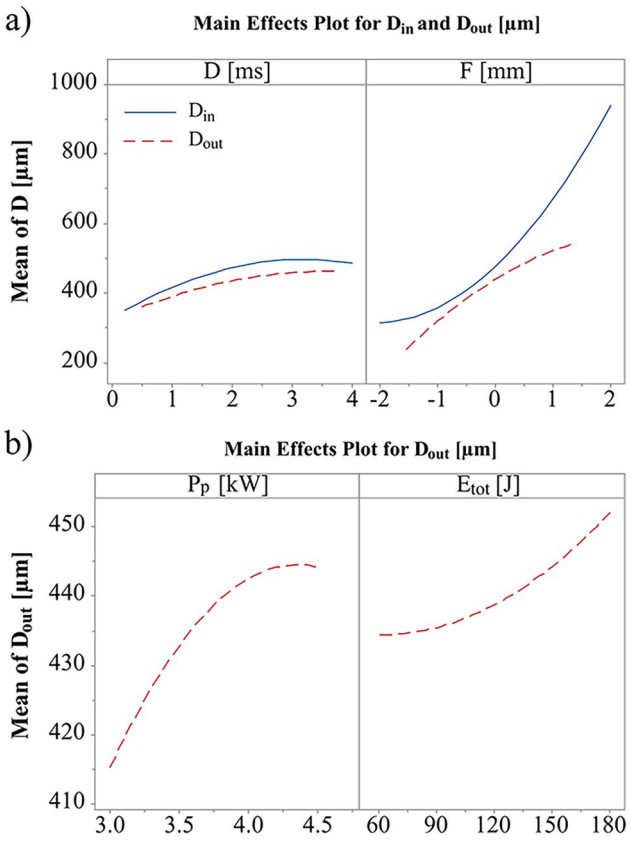

Fig. 12 Main effect plot for: **a** D_{in} and D_{out}; b) D_{out}

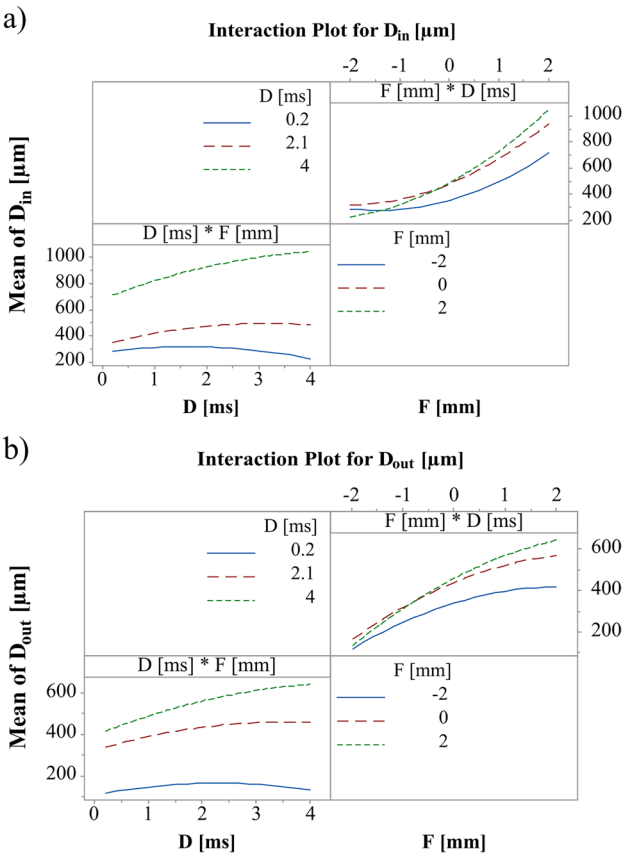

Fig. 13 Interaction plot for: **a** D_{in}; **b** D_{out}

in Fig. 12, when the duration varies, D_{in} increases more rapidly than D_{out}. When the focus varies, the difference between the two diameters presents a minimum for the focus between − 0.6 and 0 mm. Consequently, when the duration increases, the angle tends to increase; while when the focus position increases, the Ta presents a reduction followed by a subsequent increase. It is worth noting that since the D_{in} is affected only by D, F, and the D_{out} is also affected by the P_p and E_{tot}, it is possible to make small corrections to D_{out} without changing D_{in}. This, in theory, should allow obtaining a low taper angle even for diameters different from those obtainable where the difference between the two diameters achieves the minimum value (i.e. in the range of Fig. 12).

Figure 15 shows the main effect plots for R_{in}, R_{out}, Spatter, and Dross. From Fig. 15a, R_{in} decreases as D increases, and increases as F increases. R_{out} also increases as F increases with a linear trend, Fig. 15b. It should be noted that, comparing the roundness values at the entrance and exit without considering the relative diameters, it seems that the entrance hole is always worse than the exit hole. However, the difference between the mean values (and the points in the figures) of the two roundness is mainly due to the high values of R_{in} observed for high values of D_{in}, as visible in Fig. 16a. Moreover, if the percentage error is considered (similarly to what was done for the holes made in AM) the error percentage of the entrance holes (on average larger than those at the exit) is greater than the percentage error for those at the exit, as visible in Fig. 16b, where the distribution of the error percentage is reported for the two position. This means that for the same diameter value, the hole regularity is greater at the hole's entrance than at its exit.

Concerning the spatter, Fig. 15c, it is generated in the early stages of the hole, when the latter is not yet completed. The spatter decreases at the P_p increase and increases at the D and F decrease. The dross shows a similar behaviour, Fig. 15d. The increase in P_p causes an increase in the pressure generated in the plasma and, therefore, an increase in the material quantity expelled far away. Consequently, molten and resolidified material dimension (i.e. the spatter area) decreases as the peak power increases. Conversely, the increase in F or D, causes an enlargement of the area affected by fusion (D_{in} increases in both cases, Fig. 12). This determines an increase in spatter dimension. The decrease in dross as the duration increases is due to the greater overheating experienced by the molten material. Consequently, the material is more fluid and less viscous, then, it tends to be removed more easily. On the contrary, since the increase in F or E_{tot} results in a D_{out}

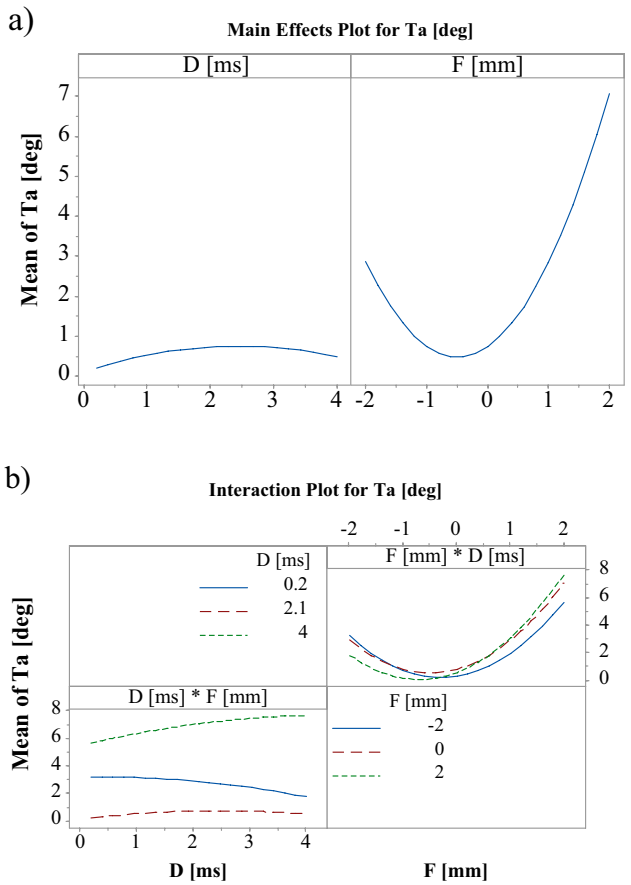

Fig. 14 Taper Angle: **a** Main effect plot; **b** Interaction plot

enlargement, there is a greater quantity of molten material (see Fig. 12) that solidifies at the hole exit, leading to a higher dross height.

4 Discussion

4.1 Comparison between the laser drilling and the AM process

In Figs. 17 and 18, the comparison between the characteristics of the holes made by laser percussion (irrespective of the process parameters) and the ones additively manufactured in terms of roundness and taper angle as a function of the actual diameter is reported. From the figures, for large diameters (close to 1 mm), the laser process results in high roundness and taper angle values. While, for additively manufactured holes the taper angle is always less than 2 degrees, regardless of the nominal diameter. Furthermore, since in laser drilling, the focus position strongly influences the diameters, the holes obtained by laser percussion show large data dispersion in terms of taper angle ranges (up to 9 degrees). It is worth noting that holes 1 mm in diameter are

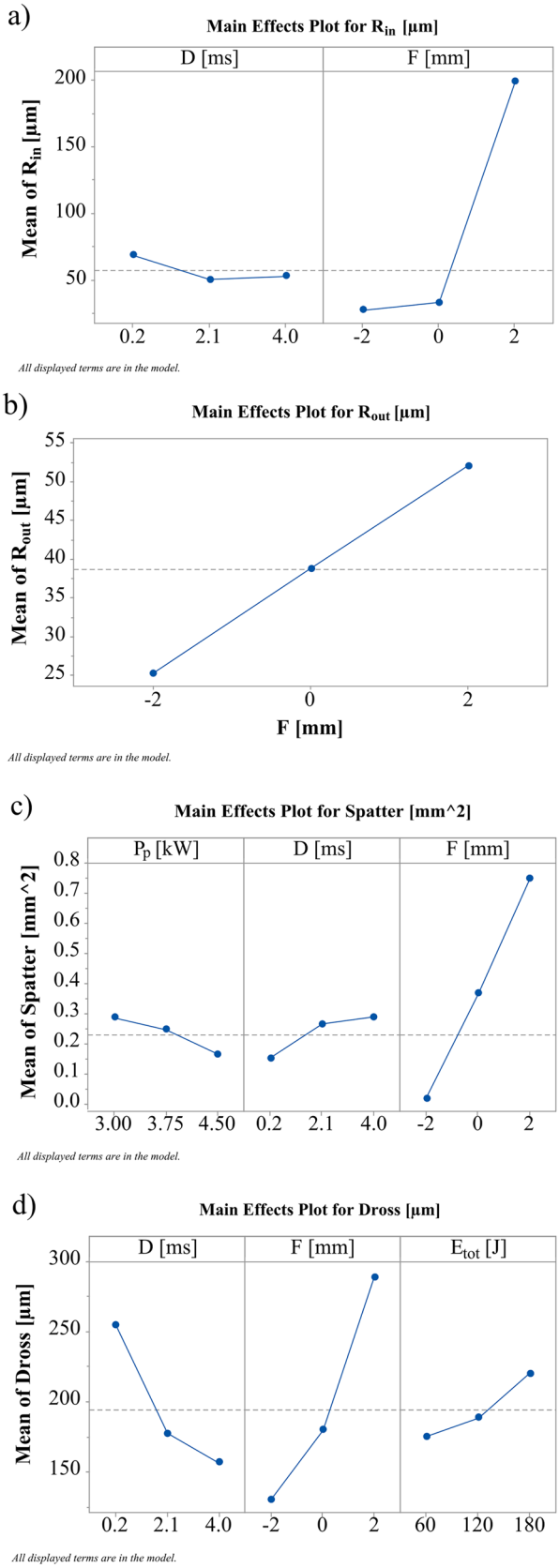

Fig. 15 Main effect plot for: **a** R_{in}; **b** R_{out}; **c** Spatter; **d** Dross

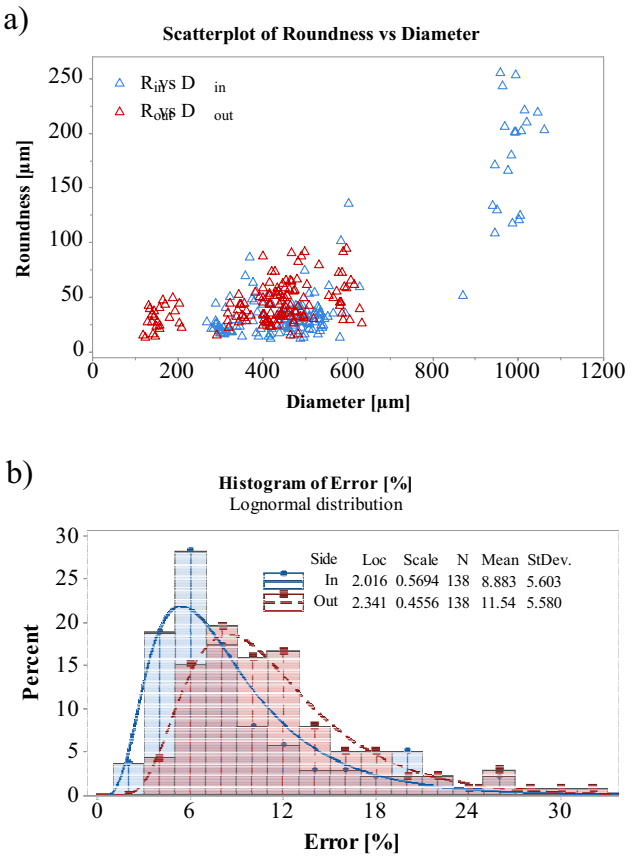

Fig. 16 **a** Scatterplot of roundness vs diameter, and **b** Histogram of Lognormal distribution of the Error [%] for laser drilled holes

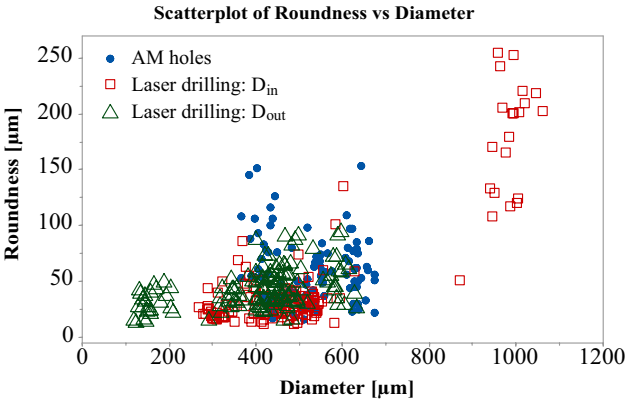

Fig. 17 Scatterplot of Roundness vs Diameter, Comparison of Laser Drilling Process (open dots) and AM (closed dots)

close to the typical laser percussion upper limit. As a matter of fact, if the kerf produced by the laser is less than 2.5 times the required hole's diameter, it can be easily obtained by the laser trepanning technique (i.e. through the central piercing and circular interpolation). On the contrary, within the diameter range of 300 µm to 450 µm, there are several points

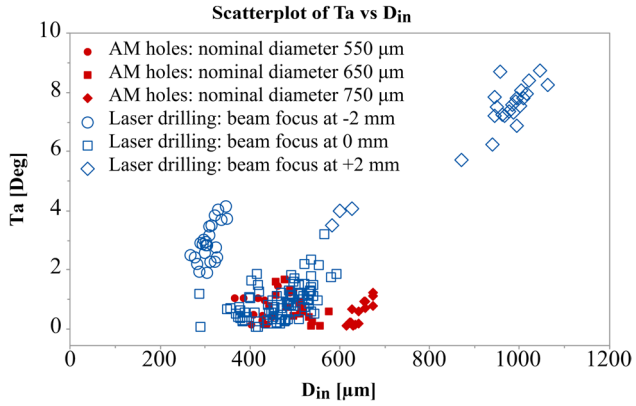

Fig. 18 Scatterplot of Taper Angle vs Diameter, Comparison of Laser Drilling Process (open dots) and AM (close dots)

(holes) obtained by laser machining, which have roundness and taper angle better than those additively manufactured.

Then, comparing the two methodologies and considering what has been illustrated, it can be deduced that, compared to AM, laser percussion drilling may be more competitive in terms of characteristics for small holes (<450 µm). On the contrary, for larger holes, on the order of a millimetre, since the taper angle is independent of the diameter, and the circularity error, due to the attachment of free particles to the hole's profile, decreases as the diameter increases (see Fig. 6b), AM technology should prevail over laser technology. Considering as aforementioned, to deepen the comparison between the two technologies, four diameters have been identified to be made using laser technology to verify whether what has just been said is true, and if the model allows for the prediction of the optimal process conditions to obtain a hole with a given diameter. In detail, two diameters were selected in the laser drilling optimal range: 300 µm and 400 µm; and two outside the range: 500 µm and 600 µm. Then, a multi-parametric optimisation technique was adopted to determine the process conditions, as described in the next paragraph.

4.2 Laser processing optimisation and model validation

Since the target of a machining process is to produce a hole with a designed geometry (in terms of diameter and roundness), low spatter and dross, and a taper angle as close as possible to zero, all together in a shorter time (here 1 s), the optimisation process must consider all the requirements at the same time. This problem is known as multi-objective process optimisation. For the optimisation, the Multi-Response Optimization (MRO) method was adopted. The method adopts the RSM equations (Table 10) to find, within the explored domain, the process conditions that allow the

target requirement. At first, the individual desirability index (di) for each response variable according to the target to be obtained (min, max or a target value) is defined as the measure of how much the response variable value (calculated by the RSM equations) deviates from the target (1 it means that the target is achieved, 0 it means that the value is far away to the target). The individual desirability values indicate how close the predicted responses are to the target requirements. The individual desirability index can be calculated according to the equations:

Target definition	Condition	di value	
Min	$RV_{model} < RV_{min}$	$di = 1$	(16)
	$RV_{model} > RV_{min}$	$di = RV_{min}/RV_{model}$	
Max	$RV_{model} < RV_{max}$	$di = RV_{model}/RV_{max}$	(17)
	$RV_{model} > RV_{max}$	$di = 1$	
Target value	$RV_{model} < RV_{target}$	$di = RV_{model}/RV_{target}$	(18)
	$RV_{model} = RV_{target}$	$di = 1$	
	$RV_{model} > RV_{target:}$	$di = RV_{target}/RV_{model}$	

where the term "RV" represents the considered response variable, RV_{model} is the value calculated by the equations of Table 10, RV_{min} is the minimum value of RV measured in the tests, RV_{max} is the maximum value of RV measured in the tests, RV_{target} is the desired value (selected between the minimum and maximum model values).

Since the models of the Roundness, Spatter and Dross show a low value of the R-sq indexes, they were discharged from the optimisation, and the D_{in}, D_{out} and Ta were adopted selecting four levels for the diameters ($D_{in} = D_{out} = 300$ µm, 400 µm, 500 µm, and 600 µm, respectively) and one level (0 deg.) for the taper angle.

The next step involves the definition of the Overall Desirability index (DI), which combines all the individual desirability (di) in a single index, here calculated by adopting the multiplicative model (the geometric mean) described in [57, 58] and reported in the following equations:

$$DI = (di_1 \cdot di_2 \cdot di_3 \ldots)^{1/n} \quad (19)$$

where the term di_n indicates the individual desirability for each response variable and n is the number of response variables ($D_{in,}$ D_{out}, Ta). DI is measured on a 0–1 scale. The optimal solution occurs where overall desirability achieves its maximum. Then, if the estimated responses (D_{in}, D_{out}, Ta) are continuous functions of the control factors (as per the equations in Table 10), it follows that di and DI are also continuous functions. Thus, univariate techniques can be adopted to maximise DI over the independent variable domain [58]. By default, the software places equal importance on the responses and assigns each an importance value of one. However, it is possible to allow some responses to have more influence on the overall desirability than other responses by setting the importance relative (i.e. the weight) on a response concerning the other. In the present case, four different runs were executed changing the diameters and the taper angle as targets and fixing the weight (importance) at 1 for all the response variables. Table 11 summarises the imposed values. It is worth noting that by imposing $D_{in} = D_{out}$, the conditions $Ta = 0$ should already be satisfied. However, in the various pre-runs performed during the identification of the optimal target setting (comprises tests containing more response variables), this condition did not provide satisfactory results (high Ta and low DI), therefore, it was preferred to also add Ta as a response to be optimised.

Table 11 Response optimisation: imposed values D_{in} [µm]; D_{out} [µm]; Ta [deg]

Run	Response	Target	Lower[a]	Upper[b]
1	D_{in} [µm]	300	267.000	1061.00
	D_{out} [µm]	300	117.000	632.00
	Ta [deg]	0	-1.165	8.72
2	D_{in} [µm]	400	267.000	1061.00
	D_{out} [µm]	400	117.000	632.00
	Ta [deg]	0	-1.165	8.72
3	D_{in} [µm]	500	267.000	1061.00
	D_{out} [µm]	500	117.000	632.00
	Ta [deg]	0	-1.165	8.72
4	D_{in} [µm]	600	267.000	1061.00
	D_{out} [µm]	600	117.000	632.00
	Ta [deg]	0	-1.165	8.72

[a]Minimum within all measured values

[b]Maximum within all measured values

For each run, 4 solutions were required, and the best one (i.e., the one with the highest desirability) was adopted in the validation tests. In Table 12, the best solutions, in terms of process parameters and estimated response variables, are reported. From the table, the optimisation provides a reasonable response for diameter values lower than 500 µm ($DI > 0.97$). While it does not find process parameter values that satisfy the conditions imposed for the diameter of 600 µm ($DI = 0.84$). This result is not unexpected since for diameters greater than 500 µm and within the investigated testing conditions, as previously highlighted, the laser drilling results in high roundness and taper angle.

Then, validation tests were carried out to verify the model and the capability of the laser drilling process. To this end, four series of ten holes, produced at the conditions indicated by Table 12, were carried out and measured. During these tests, an anti-spatter (CRC Anti-Spatter F) was successfully adopted. Table 13 and Fig. 19 summarise the results of the validation test. In the latter, the values estimated by the MRO for target diameters of 300 µm, 400 µm, 500 µm, and 600 µm were added to show the process behaviour. Comparing the experimental data to the model ones, since the

Table 12 Response Optimisation: proposed solution

Run	P_p [kW]	D [ms]	G_p [bar]	F [mm]	E_{tot} [J]	D_{in} [µm]	D_{out} [µm]	Ta [deg]	DI
1	3.83	4.00	8.09	− 1.08	148.49	300.05	300.15	0.01	1.00
2	4.15	0.74	13.00	0.02	147.27	419.76	399.42	0.39	0.97
3	3.83	4.00	7.00	0.09	76.97	500.01	480.46	0.37	0.97
4	4.39	1.58	13.00	0.75	120.61	600.00	494.19	2.01	0.84

Table 13 Comparison between the values estimated by the MRO and the experimental ones

Run	Response	Model estimation			
		Fit	95% CI		95% CI
	D_{in} [µm]	300.0	262.6; 337.5	309.2	290.1—328.3
	D_{out} [µm]	300.15	281.43; 318.88	308.3	291.2—325.4
	Ta [deg]	0.006	− 0.646; 0.657	-0.159	-0.439—0.120
	D_{in} [µm]	419.8	381.1; 458.5	453.4	443.7—463.0
	D_{out} [µm]	399.42	380.07; 418.77	402.5	395.8—409.2
	Ta [deg]	0.390	− 0.284; 1.063	0.865	0.636—1.093
	D_{in} [µm]	500.0	452.2; 547.8	477.2	467.8—486.5
	D_{out} [µm]	480.5	456.6; 504.4	454.1	449.2—458.9
	Ta [deg]	0.371	− 0.461; 1.203	0.366	0.187—0.546
	D_{in} [µm]	600.0	562.7; 637.4	607.8	563.4—652.2
	D_{out} [µm]	494.19	475.52; 512.86	482.7	466.3—499.0
	Ta [deg]	2.011	1.361; 2.661	2.392	1.776—3.007

average values are very close and the confidence interval bars overlap, a good agreement between the model and the experimental data is confirmed. Nevertheless, for diameters greater than 500 µm, the exit hole tends to be narrow. It is important to highlight that this limitation is mainly due to the test conditions (particularly the imposition of a maximum duration of one second on the process) rather than the model itself.

Figures 20 and 21 show images of the entry side, exit side, and section of holes obtained under the RMS optimal conditions. Compared to the additively manufactured holes, the ones obtained by laser percussion in the diameter interval of 300–600 µm show a more regular geometry concerning inlet and outlet diameters and section profiles. This is also confirmed by the Error [%] index values measured on these holes, Fig. 22, which are always lower than those of the AM's holes (see also Fig. 6).

In conclusion, considering the possibility of having a low diameter (300 µm), a low taper angle (< 4 deg.), and a better Error [%] in a very short process time (1 s), the outcome appears very promising.

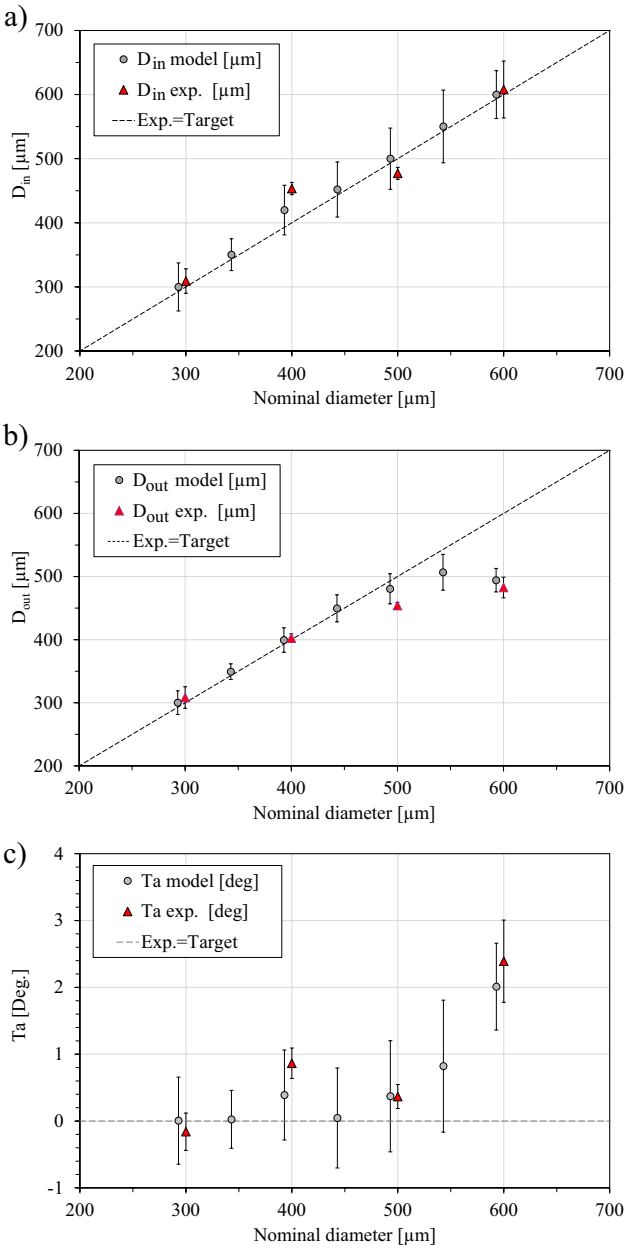

Fig. 19 Comparison between model optimal solution and experimental data for **a** D_{in}; **b** D_{out}; **c** Ta. In the graph, the bars indicate the 95% Confidence Interval

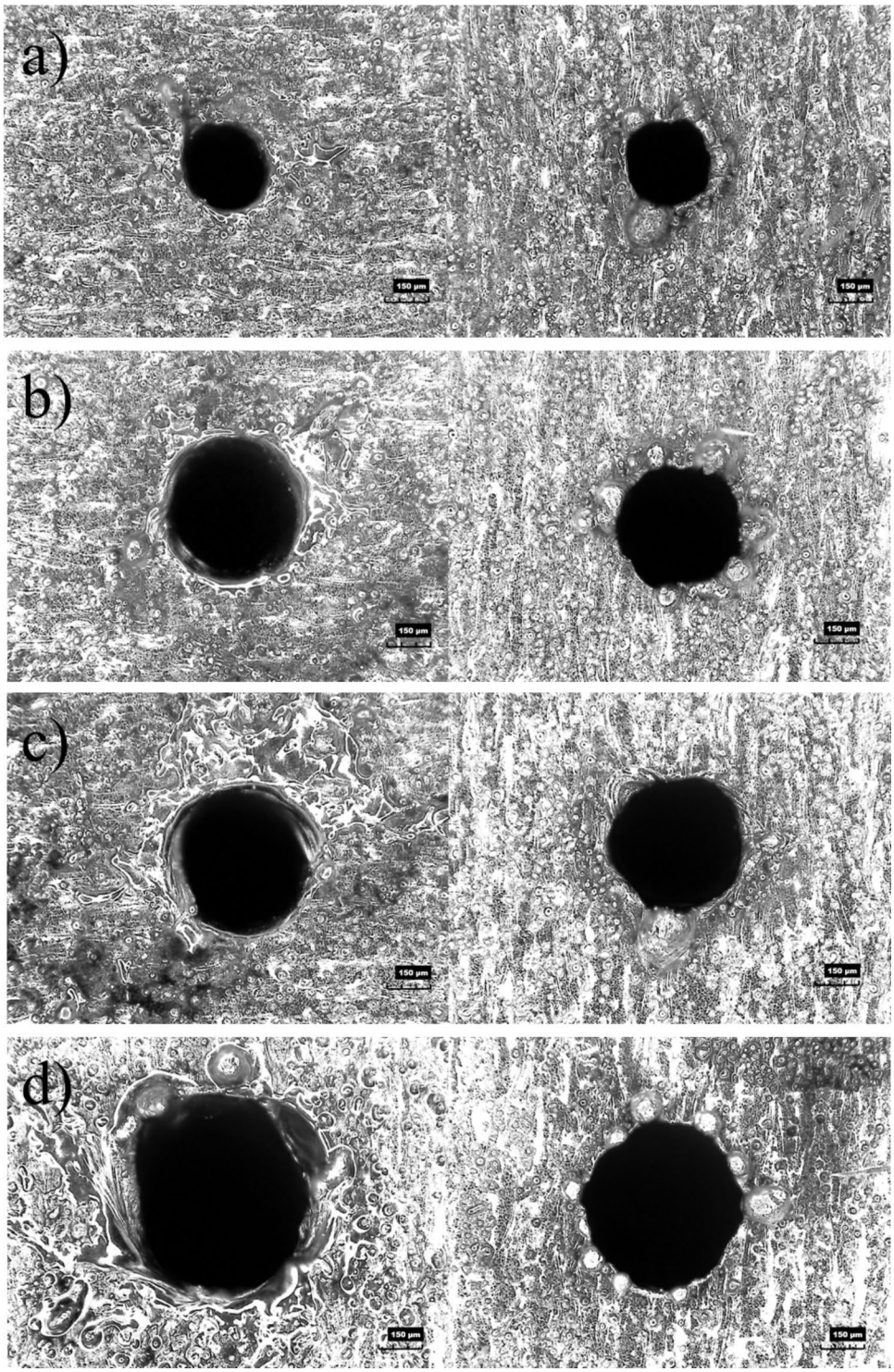

Fig. 20 Images of the optimised holes at the laser input (@ left) and output (@ right) sides, for the diameters of: **a** 300 µm; **b** 400 µm; **c** 500 µm; **d** 600 µm

5 Conclusion

The present work adopts a 450/4500 QCW fiber laser to drill a CoCrMo alloy plate produced by additive manufacturing by the percussion drilling method. Experimental tests were performed adopting a Box-Behnken design. During the tests, the pulse power, pulse duration, assistant gas pressure, focus position, and total released energy were varied. The inlet and outlet diameters, their circularity, and the spatter and dross dimensions were measured. ANOVA and RSM were adopted to investigate the effect of the process parameters and to model the process. The characteristics of the laser-drilled holes were compared to additively manufactured ones. Finally, MRO was adopted to optimise the process

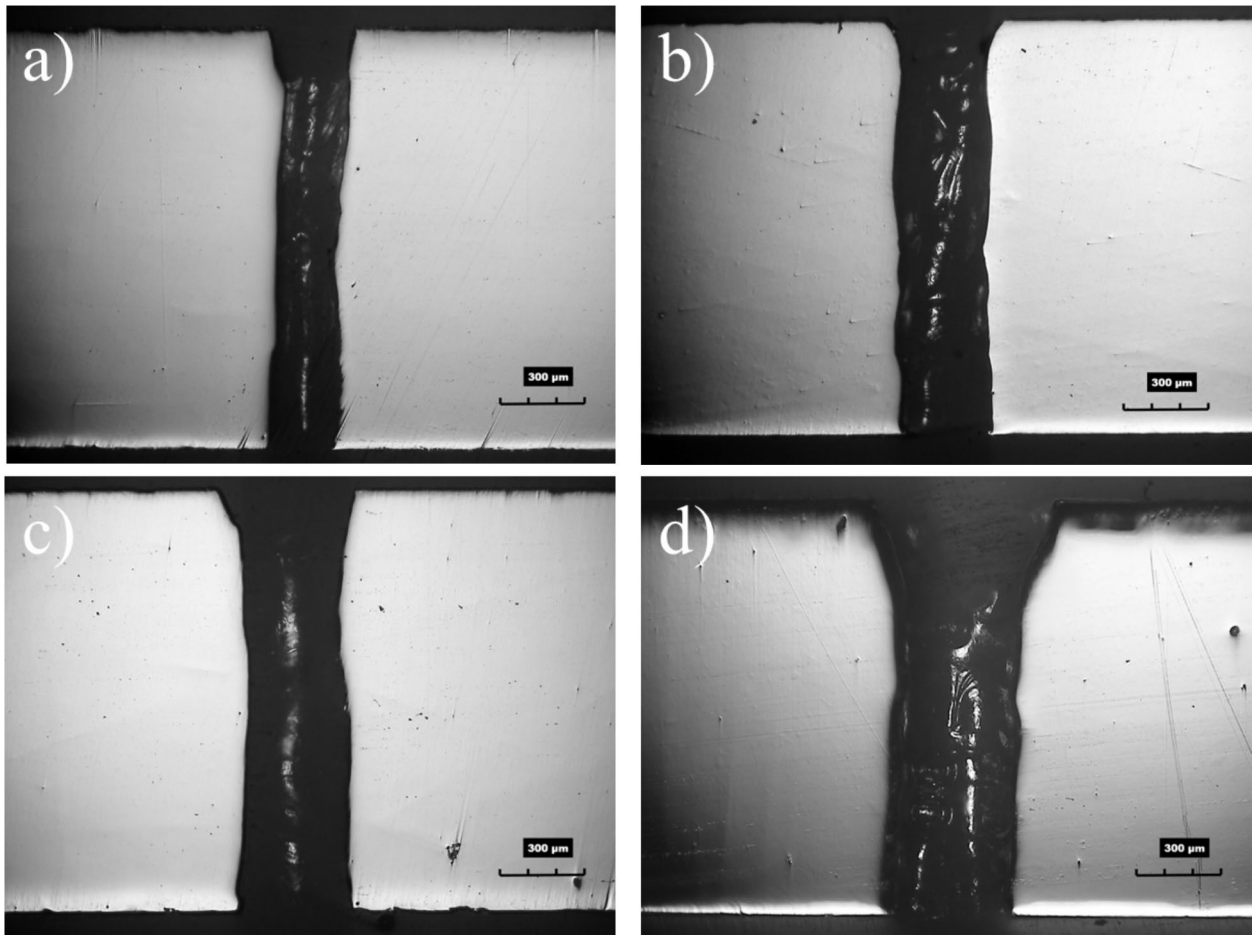

Fig. 21 Images of the sections of the optimised holes, for the diameters of: **a** 300 µm; **b** 400 µm; **c** 500 µm; **d** 600 µm

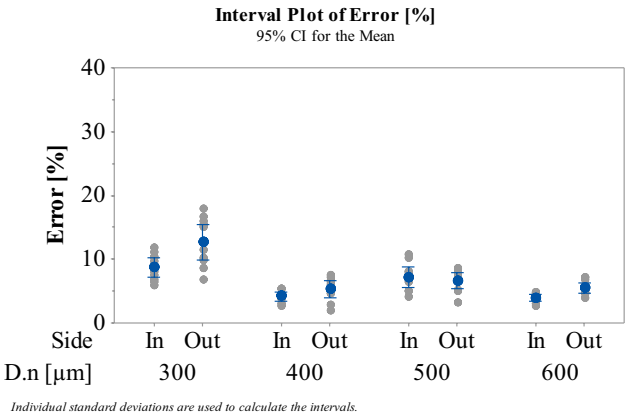

Fig. 22 Error [%] measured on the validation test holes. (D.n = nominal diameter)

conditions to obtain holes with a small diameter (< 400 µm). From the results, within the adopted source, material, and process conditions, the following main conclusions were drawn:

- The additively manufactured holes are affected by several defects such as diameters smaller than the nominal value, high roundness values, and elliptical shape.
- These defects are mainly due to the adopted technology and to the down-skin problem, the latter consists of the particles or particle clusters attachment to the vault of the hole.
- These defects increase as the hole diameter decreases, limiting, in fact, the possibility of producing micro-holes directly during the manufacturing of the component.
- The laser percussion drilling technique offers high flexibility concerning the hole characteristics since diameters in the range of 300 µm to 1000 µm can be obtained. This theoretically allows the diameter to be varied within these values.
- Among the parameters analysed, the main significant parameter is the beam focus position which affects all the parameters and shows the highest F-value, followed by the pulse duration.

- Peak power and total energy play a secondary role, with the former affecting D_{out} and spatter, and the latter influencing spatter and dross.
- The assist gas pressure does not appear to affect any geometric variables.
- By comparing the experimental data of laser drilling and those of holes made directly during the AM process, it shows that the laser percussion technique can make holes with better geometric characteristics (Ta, R_{in}, R_{out}) in the range of 300–500 µm in diameter.
- Response Surface Methodology (RSM) can model both the diameters and the taper angle. Conversely, roundness, spatter, and dross models show a large model error.
- The Multi Response Optimisation (MRO) technique was adopted to optimise the process condition and obtain holes with different imposed diameters and minimum taper angles.
- The direct comparison between the model estimation and the experimental measures showed a good agreement at least up to 600 µm in diameter.

6 Conflict of interest

The authors declare no competing interests.

Acknowledgements The authors are particularly grateful to the Interuniversity Research Centre CIRTIBS for the equipment to develop the present research work.

Author contributions All persons who meet authorship criteria are listed as authors, and all authors certify that they have participated sufficiently in the work to take public responsibility for the content, including participation in the concept, design, analysis, writing, or revision of the manuscript. Furthermore, each author certifies that this material or similar material has not been and will not be submitted to or published in any other publication. D.M.: Data curation, Formal analysis, Investigation, Methodology, Resources, Writing-Original draft preparation, Writing-Reviewing and Editing. S.G.: Formal analysis, Investigation, Methodology, Writing-Reviewing and Editing. C. L.: Conceptualisation, Data curation, Formal analysis, Investigation, Methodology, Resources, Writing-Original draft preparation, Writing-Reviewing and Editing.

Funding Open access funding provided by Università degli Studi della Campania Luigi Vanvitelli within the CRUI-CARE Agreement.

Data availability No datasets were generated or analysed during the current study.

References

1. Frazier WE (2014) Metal additive manufacturing: a review. J Mater Eng Perform 23:1917–1928. https://doi.org/10.1007/s11665-014-0958-z
2. Moeinfar K, Khodabakhshi F, Kashani-bozorg SF, Mohammadi M, Gerlich AP (2022) A review on metallurgical aspects of laser additive manufacturing (LAM): Stainless steels, nickel superalloys, and titanium alloys. J Mater Res Technol 16:1029–1068. https://doi.org/10.1016/j.jmrt.2021.12.039
3. Lewandowski JJ, Seifi M (2016) Metal additive manufacturing: a review of mechanical properties. Annu Rev Mater Res 46:151–186. https://doi.org/10.1146/annurev-matsci-070115-032024
4. Contuzzi N, Campanelli SL, Caiazzo F, Alfieri V (2019) Design and fabrication of random metal foam structures for laser powder bed fusion. Materials (Basel). https://doi.org/10.3390/ma12081301
5. Campanelli SL, Contuzzi N, Ludovico AD, Caiazzo F, Cardaropoli F, Sergi V (2014) Manufacturing and characterization of Ti6Al4V lattice components manufactured by selective laser melting. Materials (Basel) 7:4803–4822. https://doi.org/10.3390/ma7064803
6. Bourell D, Kruth JP, Leu M, Levy G, Rosen D, Beese AM, Clare A (2017) Materials for additive manufacturing. CIRP Ann - Manuf Technol 66:659–681. https://doi.org/10.1016/j.cirp.2017.05.009
7. Herzog D, Seyda V, Wycisk E, Emmelmann C (2016) Additive manufacturing of metals. Acta Mater 117:371–392. https://doi.org/10.1016/j.actamat.2016.07.019
8. R.W. Revie, H.H. Uhlig, 2008 Cobalt and Cobalt Alloys. In: Corros Control, Wiley, pp. 419–423. https://doi.org/10.1002/9780470277270.ch24.
9. Béreš M, Silva CC, Sarvezuk PWC, Wu L, Antunes LHM, Jardini AL, Feitosa ALM, Žilková J, de Abreu HFG, Filho RM (2018) Mechanical and phase transformation behaviour of biomedical Co-Cr-Mo alloy fabricated by direct metal laser sintering. Mater Sci Eng A 714:36–42. https://doi.org/10.1016/j.msea.2017.12.087
10. Gatto A, Iuliano L, Calignano F, Bassoli E (2012) Electrodischarge drilling performance on parts produced by DMLS. Int J Adv Manuf Technol 58:1003–1018. https://doi.org/10.1007/s00170-011-3446-8
11. Girardin E, Barucca G, Mengucci P, Fiori F, Bassoli E, Gatto A, Iuliano L, B. (2016) Rutkowski Biomedical Co-Cr-Mo Components Produced by Direct Metal Laser Sintering. Mater Today Proc. Elsevier Ltd, Amsterdam, pp 889–897. https://doi.org/10.1016/j.matpr.2016.02.022
12. Kumar P, Sawant MS, Jain NK, Gupta S (2022) Study of mechanical characteristics of additively manufactured Co-Cr-Mo-2/4/6Ti alloys for knee implant material. CIRP J Manuf Sci Technol 39:261–275. https://doi.org/10.1016/j.cirpj.2022.08.015
13. Li J, Shi W, Lin Y, Li J, Liu S, Liu B (2023) Comparative study on MQL milling and hole making processes for laser beam powder bed fusion (L-PBF) of Ti-6Al-4V titanium alloy. J Manuf Process 94:20–34. https://doi.org/10.1016/j.jmapro.2023.03.055
14. Min Z, Wu Y, Yang K, Xu J, Parbat SN, Chyu MK (2021) Dimensional characterizations using scanning electron microscope and surface improvement with electrochemical polishing of additively manufactured microchannels. J. Eng Gas Turbines Power. DOI 10(1115/1):4049908

15. Wang S, Liu Y, Shi W, Qi B, Yang J, Zhang F, Han D, Ma Y (2017) Research on high layer thickness fabricated of 316L by selective laser melting. Materials (Basel). 10:1055. https://doi.org/10.3390/ma10091055
16. Furgeson MT, Veley EM, Yoon C, Gutierrez D, Bogard DG, Thole KA (2025) Development and Evaluation of Shaped Film Cooling Holes Designed for Additive Manufacturing. Proc ASME Turbo Expo. American Society of Mechanical Engineers (ASME), Rotterdam, p V06AT12A041. https://doi.org/10.1115/GT2022-83201
17. Castelli N, Picchi A, Facchini B, Winchler L, Morante F (2024) Optimization of a Novel Design-For-Additive-Manufacturing Film Cooling Hole. Proc ASME Turbo Expo, American Society of Mechanical Engineers (ASME). Uk, London, p V007T12A039
18. Dedeakayogulları H, Kacal A (2022) Experimental investigation of hole quality in drilling of additive manufacturing Ti6Al4V parts produced by hole features. J Manuf Process 79:745–758. https://doi.org/10.1016/j.jmapro.2022.04.039
19. Boban J, Ahmed A (2023) Defect mitigation and surface enhancement of additively manufactured AlSi10Mg internal features using electro-thermal post-treatment. Mater Lett. https://doi.org/10.1016/j.matlet.2023.135267
20. Joshy J, Kuriachen B (2023) Influence of post-processing and build orientation on the micro-machinability and chip formation during micro-drilling of L-PBF AlSi10Mg. CIRP J Manuf Sci Technol 45:35–48. https://doi.org/10.1016/j.cirpj.2023.05.009
21. Pimenov DY, Berti LF, Pintaude G, Peres GX, Chaurasia Y, Khanna N, Giasin K (2023) Influence of selective laser melting process parameters on the surface integrity of difficult-to-cut alloys: comprehensive review and future prospects. Int J Adv Manuf Technol 127:1071–1102. https://doi.org/10.1007/s00170-023-11541-8
22. Sorgato M, Zanini F, Bertolini R, Ghiotti A, Bruschi S (2020) Improvement of micro-hole precision by ultrasound-assisted drilling of laser powder bed fused Ti6Al4V titanium alloy. Precis Eng 66:31–41. https://doi.org/10.1016/j.precisioneng.2020.06.014
23. Karabulut Y, Kaynak Y (2020) Drilling process and resulting surface properties of Inconel 718 alloy fabricated by Selective Laser Melting Additive Manufacturing. Procedia CIRP. Elsevier BV, Amsterdam, pp 355–359
24. Rysava Z, Bruschi S, Carmignato S, Medeossi F, Savio E, Zanini F (2016) Micro-drilling and Threading of the Ti6Al4 v Titanium Alloy Produced through Additive Manufacturing. Procedia CIRP. Elsevier BV, Amsterdam, pp 583–586
25. Singh E, Singh AK, Reddy RDP, Sharma V (2023) Drilling strategies for additively manufactured and casted SS316L stainless steel. J Mater Eng Perform. https://doi.org/10.1007/s11665-023-09005-x
26. Deepu P, Jagadesh T (2024) A review on short and ultrashort pulsed laser microdrilling: materials mechanism, methods and applications. J Brazilian Soc Mech Sci Eng. https://doi.org/10.1007/s40430-024-04992-x
27. Fornaroli C, Holtkamp J, Gillner A (2013) Laser-beam helical drilling of high quality micro holes. Phys Procedia 41:661–669. https://doi.org/10.1016/j.phpro.2013.03.130
28. Duan W, Mei X, Fan Z, Chen J, Zhang Y (2020) Dynamic change process of a recast layer in Nd:YAG millisecond laser trepan drilling. J Opt Soc Am B Opt Phys 37:804–812. https://doi.org/10.1364/JOSAB.380129
29. Marimuthu S, Antar M, Dunleavey J (2019) Characteristics of micro-hole formation during fibre laser drilling of aerospace superalloy. Precis Eng 55:339–348. https://doi.org/10.1016/j.precisioneng.2018.10.002
30. Low DKY, Li L, Corfe AG, Byrd PJ (2001) Spatter-free laser percussion drilling of closely spaced array holes. Int J Mach Tools Manuf 41:361–377
31. Moradi M, Golchin E (2017) Investigation on the effects of process parameters on laser percussion drilling using finite element methodology; statistical modelling and optimization. Lat Am J Solids Struct 14:464–484. https://doi.org/10.1590/1679-78253247
32. Mishra S, Yadava V (2013) Modeling and optimization of laser beam percussion drilling of nickel-based superalloy sheet using Nd: YAG laser. Opt Lasers Eng 51:681–695. https://doi.org/10.1016/j.optlaseng.2013.01.006
33. Low DKY, Li L, Byrd PJ (2000) The effects of process parameters on spatter deposition in laser percussion drilling. Opt Laser Technol 32:347–354
34. Low DKY, Li L, Byrd PJ (2003) Spatter prevention during the laser drilling of selected aerospace materials. J Mater Process Technol 139:71–76. https://doi.org/10.1016/S0924-0136(03)00184-5
35. Low DKY, Li L, Corfe AG (2000) Effects of assist gas on the physical characteristics of spatter during laser percussion drilling of NIMONIC 263 alloy. Appl Surf Sci 154:689–695
36. Nawaz S, Kashif M, Abbas N, Farooq M, Farhan M, Amjad M, Noor F, Naqvi RA (2020) Effect of defocused plane on entrance and exit hole geometry of high grade steel 18CrNi8 during percussion drilling by Nd:YAG millisecond laser system. Mater Res Exp. https://doi.org/10.1088/2053-1591/ab654c
37. Manninen M, Hirvimäki M, Matilainen VP, Salminen A (2017) Comparison of laser-engraved hole properties between cold-rolled and laser additive manufactured stainless steel sheets. Appl Sci. https://doi.org/10.3390/app7090913
38. Hagenlocher C, Henn M, Buser M, Cirakoglu K, Michel J, Onuseit V, Graf T (2024) Exceeding the limits of conventional manufacturing by means of combining additive and subtractive material processing with cw-And ultrafast lasers. In: Habi S (ed) Procedia CIRP. Elsevier BV, Amsterdam, pp 153–156. https://doi.org/10.1016/j.procir.2024.08.089
39. EOS, 3D Printing Cobalt Crome MP1 (n.d.). https://www.eos.info/metal-solutions/metal-materials/cobalt-chrome (accessed October 14, 2024).
40. EOS, EOS Cobalt Crome MP1 Process Data Sheet, (n.d.). https://www.eos.info/var/assets/05-datasheet-images/Assets_MDS_Metal/EOS_CobaltChrome_MP1/Material_DataSheet_EOS_CobaltChromeMP1_en.pdf?v=7 (accessed June 25, 2025).
41. EOS, EOS Cobalt Crome MP1 Powder Data sheet, (n.d.). https://www.eos.info/metal-solutions/metal-materials/data-sheets/mds-eos-cobalt-chrome-mp1 (accessed June 25, 2025).
42. Ready JF, J. F., D.F. Farson, T. Feeley, (2001) LIA Handbook of Laser Materials Processing. Springer-Verlag, Berlin Heidelberg
43. M. Mendes, R. Sarrafi, J. Schoenly, R. Vangemert, Fiber laser micromachining in high-volume manufacturing, Laser Focus World. (2015). https://www.laserfocusworld.com/industrial-laser-solutions/article/14216389/fiber-laser-micromachining-in-highvolume-manufacturinganufacturing.pdf (accessed June 25, 2025).
44. T. Hoult, Maybe the most flexible laser—ever!, Laser Focus World. (2015). https://www.laserfocusworld.com/industrial-laser-solutions/article/14216362/maybe-the-most-flexible-laser ever (accessed June 25, 2025).
45. J. Dietrich, I. Kelbassa, Drilling with fiber lasers, Laser Focus World. (2012). https://www.laserfocusworld.com/industrial-laser-solutions/article/14216221/drilling-with-fiber-lasers (accessed June 25, 2025).
46. Montgomery DC (2019) Design and analysis of experiments, 10th edn. Wiley, New York, NY

47. Coleman DE, Montgomery DC (1993) A systematic approach to planning for a designed industrial experiment. Technometrics 53:1–12. https://doi.org/10.1080/00401706.1993.10484984
48. R. Walkers, D. Havrilla, Process Fundamentals of Industrial Laser Welding and Cutting, II, Rofin-Sinar, Plymount, Michigan, 1999.
49. Ferreira SLC, Bruns RE, Ferreira HS, Matos GD, David JM, Brandão GC, da Silva EGP, Portugal LA, dos Reis PS, Souza AS (2007) Box-Behnken design: An alternative for the optimization of analytical methods. Anal Chim Acta 597:179–186. https://doi.org/10.1016/j.aca.2007.07.011
50. Tamilarasan A, Rajamani D (2017) Multi-response optimization of Nd:YAG laser cutting parameters of Ti-6Al-4V superalloy sheet. J Mech Sci Technol 31:813–821. https://doi.org/10.1007/s12206-017-0133-1
51. Mishra DR, Bajaj A, Bisht R (2020) Optimization of multiple kerf quality characteristics for cutting operation on carbon–basalt–Kevlar29 hybrid composite material using pulsed Nd:YAG laser using GRA. CIRP J Manuf Sci Technol 30:174–183. https://doi.org/10.1016/j.cirpj.2020.05.005
52. Arun A, Santosh S, Rajkumar K (2024) Investigations on the interaction of laser parameters for efficient microdrilling of NiTiV smart alloy system. Laser Phys 34:085101. https://doi.org/10.1088/1555-6611/ad552e
53. Calignano F, Manfredi D, Ambrosio EP, Iuliano L, Fino P (2013) Influence of process parameters on surface roughness of aluminum parts produced by DMLS. Int J Adv Manuf Technol 67:2743–2751. https://doi.org/10.1007/s00170-012-4688-9
54. Charles A, Bayat M, Elkaseer A, Thijs L, Hattel JH, Scholz S (2022) Elucidation of dross formation in laser powder bed fusion at down-facing surfaces: phenomenon-oriented multiphysics simulation and experimental validation. Addit Manuf 50:102551
55. R. Paschotta, Gaussian Beams, RP Photonic Encycl. (n.d.). https://doi.org/10.61835/enc.
56. Yilbas BS, Sami M (1996) Study into the effect of beam waist position on hole formation in the laser drilling process. Proc Inst Mech Eng Part B J Eng Manuf 210:271–277
57. Chiao CH, Mastrangelo CM (2001) Comparing methods for the multi-response design problem. Qual Reliab Eng Int 17:323–331. https://doi.org/10.1002/qre.404
58. Derringer G, Suich R (1980) Simultaneous optimization of several response variables. J Qual Technol. https://doi.org/10.1080/00224065.1980.11980968